

Two-point correlation function for a scalar field on a Schwarzschild background

Cláudia Simone Buss

DISSERTATION THESIS PRESENTED
TO THE
BRAZILIAN CENTER FOR RESEARCH IN PHYSICS
IN ORDER TO
OBTAIN THE TITLE
OF
MASTER IN SCIENCE

Program: Postgraduate Program in Physics

Orientador: Prof. Dr. Marc Casals

During the work related to this thesis, the author was beneficiary of a CNPq's scholarship.

Rio de Janeiro, August, 2016

Two-point correlation function for a scalar field on a Schwarzschild background

This thesis' version has been updated to accomodate corrections and suggestions proposed by the Awarding Committee during the defence – held on 19/08/2016. A copy of this thesis is available at the Brazilian Center for Research in Physics (CBPF).

Awarding Committee:

- Prof. Dr. Marc Casals Casanellas (advisor) - CBPF
- Prof. Dr. Sebastião Alvez Dias - CBPF
- Prof. Dr. Sérgio Eduardo de Carvalho Eyer Jorás - UFRJ

Acknowledgements

Eu começo agradecendo à minha família. Em tantos sentidos simplesmente não seria possível chegar aqui sem tê-los em minha vida.

Eu sou eternamente grata aos Professores que me formaram e formam desde a educação primária. Eu sou grata àqueles Professores que continuam a se mover, que continuam a acolher alunos e a gerar perguntas, mesmo contra um fluxo doloroso materializado no “sem partido”. Hoje eu menciono o nome do Professor Dr. Fernando de Melo, a quem agradeço as aulas que iam além dos livros e passavam pela sua experiência com pesquisa e a sua abertura a questionamentos. Agradeço também a oportunidade de participar do ensino como monitora sob seu supervisionamento.

Em particular, eu e Rio não seríamos os mesmos sem vocês, Vanessa Pacheco de Freitas Josephine Rua, Gabriel Bartosch Caminha, Clara Macedo, Marília Quezado e a Patota Feliz das Futuras Mechas Coloridas.

Agradeço ao Dr. Marc Casals, orientador desse projeto. Muito do que aprendi durante o período do meu mestrado se deve a ele. Aproveito também para agradecer ao ICRA.

Muito dessa dissertação se deve ao Governo Federal do Brasil (aquele da Pátria Educadora). Ressalto que o Governo aqui é representado, em particular, pelas escolas em que estudei, pelos Professores que me formaram, pela Universidade Federal de Santa Catarina (como graduanda), pela CAPES (enquanto graduanda bolsista do Programa Ciências sem Fronteiras), pelo Centro Brasileiro de Pesquisas Físicas, pelo CNPq (enquanto bolsista de Mestrado) e pelo MCTI, hoje extinto.

Abstract

The object of study in this thesis is a quantum massless scalar field on a Schwarzschild spacetime, under the linear approach of Quantum Field Theory on curved spacetimes. The purpose of the research in this thesis is threefold: to investigate analytically and numerically mode solutions to the wave equation satisfied by the mentioned field; calculate two-point correlation functions for the Boulware, Unruh and Hartle-Hawking quantum states in the exterior region of a Schwarzschild black hole; and pave the way to explore the entanglement between outgoing Hawking radiation and its ingoing counterpart.

The two-point functions – which depend on the mode solutions – are related to the renormalized stress-energy tensor and, more importantly to the scope of this thesis, allow to answer inquiries related to quantum correlations. Our study of the field's correlations considering points internal and external to the black hole is inspired by the study of condensed-matter analogues and lower-dimensional black holes. It also allows to retrieve field information relating the interior and exterior regions of the black hole. This fact bears importance in research topics related to the nature of these astrophysical objects, such as the information paradox.

Considering this, one of the main results obtained in this thesis is the analytical continuation of mode solutions to the region internal to the black hole's event horizon – extending previous works. The second relevant research outcome is the observation and explanation of global divergence patterns of the two-point Feynman functions, along with a successful cross-check against a well-established classical result.

In conclusion, the know-how obtained for a stable numerical implementation of the two-point functions combined with the extension of the mode solutions to the interior of the horizon will be of cornerstone importance to the study of the field's entanglement in different regions of a Schwarzschild black hole.

Keywords: Schwarzschild, black holes, Hawking radiation, massless scalar field, quantum correlations.

Resumo

O objeto de estudo dessa dissertação é um campo escalar não-massivo, que é investigado sob a luz da Teoria Quântica de Campos em espaços curvos. São três os propósitos dessa pesquisa: investigar soluções modais analítica e numericamente para a equação diferencial regendo a evolução do campo citado; calcular a função de correlação de dois pontos para os estados quânticos de Boulware, Unruh e Hartle-Hawking na região externa ao buraco negro de Schwarzschild; e fornecer o ferramental necessário para a pesquisa sobre o emaranhamento entre a radiação Hawking emitida e a sua contrapartida absorvida.

As funções de correlação de dois pontos – que dependem das soluções modais – são relacionadas ao tensor energia-momento renormalizado e permitem responder perguntas relacionadas a correlações quânticas. O estudo da correlação de um campo tomando um ponto interno ao horizonte de eventos e outro externo é inspirado por estudos de modelos análogos da matéria condensada e de modelos de buracos negros com dimensão reduzida. Essas funções de dois pontos também permitem que informação ligando regiões internas e externas ao horizonte de eventos seja recuperada. Esse fato é extremamente relevante para a compreensão da natureza desses objetos astrofísicos – por exemplo, no caso de estudos sobre o Paradoxo da Informação.

Considerando o acima dito, um dos principais resultados é a continuação analítica de soluções modais – estendendo trabalhos anteriores. O segundo resultado relevante aqui apresentado é a observação e explicação de padrões de divergência das funções de Feynman, juntamente a comparação bem-sucedida de nossos resultados numéricos com um resultado clássico já estabelecido na literatura.

Por fim, o *know-how* obtido na implementação estável do cálculo para as funções de correlação, juntamente da extensão das soluções modais para o interior do horizonte são de fundamental importância para o estudo do emaranhamento do campo nas diferentes regiões do buraco negro de Schwarzschild.

Palavras-chave: Schwarzschild, buracos negros, radiação Hawking, campo escalar não-massivo, correlações quânticas.

Contents

List of Abbreviations	ix
List of Symbols	xi
List of Figures	xiii
List of Tables	xvii
1 Introduction	1
2 Black Holes	5
2.1 Foundations of General Relativity	5
2.2 Schwarzschild Black Hole	7
2.3 Observational Evidence for Black Holes	10
3 Quantum Field Theory in Curved Spacetimes	13
3.1 Linear Approach and Quantum Field Theory in Curved Spacetimes	14
3.2 Scalar Fields	15
3.3 Semi-Classical Black Holes	19
3.4 QFT CS: Motivations and Beyond	22
4 Wave Equation and Radial Solutions	25
4.1 Separability of the Wave Equation	25
4.2 Singular Structure of the Radial Equation	28
4.3 Series Expansions	30
4.4 Calculation of In-, Out- and Upgoing Modes	33
4.4.1 Ingoing modes	35
4.4.2 Outgoing modes	37
4.4.3 Upgoing modes	37
4.5 Asymptotics	41
4.5.1 Large ωr	41
4.5.2 Exact solution, $\omega = 0$	43
4.5.3 Small $M\omega$	44

4.5.4	Candelas' asymptotics for ℓ -sum	44
5	Two-point Correlation Functions	49
5.1	Equality Between the Real Parts	50
5.2	Case-study: Singularity Structure and Caustics	53
6	Conclusions	63
A	Numerical Tests	65
	Bibliography	67

List of Abbreviations

EFE	Einstein's Field Equations
IEF	Ingoing Eddington-Finkelstein
QFT CS	Quantum Field Theory in curved spacetimes
KG	Klein-Gordon
GR	General Relativity
AdS/CFT	Anti-de Sitter/Conformal Field Theory
ODE	Ordinary Differential Equation
AGN	Active Galactic Nucleus
MST	Mano-Suzuki-Takasugi Method
RHS	Right Hand Side
LHS	Left Hand Side

List of Symbols

$g_{\mu\nu}$	spacetime metric
g	determinant of g'_{μ}
ω	Mode frequency
ℓ	Mode angular momentum number
G	Gravitational constant
c	Speed of light
\mathcal{I}^+	future null infinity
\mathcal{I}^-	past null infinity
\mathcal{H}^+	future event horizon
\mathcal{H}^-	past event horizon

List of Figures

2.1	Penrose-Carter diagram showing the (compactified) maximal extension of the Schwarzschild manifold. Region II is the black hole interior, II' is the white hole interior, while I and I' are the external regions. \mathcal{H}^+ and \mathcal{H}^- are the future and past event horizons, respectively. \mathcal{J}^+ and \mathcal{J}^- , future and past null infinities. I^+ and I^- are the future and past timelike infinities, while I^0 are the spacelike infinities. Finally, $r = 0$ represent the curvature singularities. A massive particle in region I of a non-eternal Schwarzschild black hole would typically start its trajectory at region I^- and either end up at I^+ without entering the black hole or else cross, perhaps, the future event horizon \mathcal{H}^+ entering region II. Image's credit to [39].	9
3.1	Ingoing and upgoing modes in Region I of a maximally extended Schwarzschild spacetime. Credit to [39].	17
4.1	Plots of the dimensionless Fröbenius coefficients for the $\alpha = 0$, $\sigma = -1$, $\omega = 1.42618/M$	32
4.2	Ingoing radial function. Dashed lines correspond to the real part of the radial function, while continuous lines correspond to the imaginary part. $\alpha = 0$. Here, we used our Fröbenius expansion in the interval $r \in (2M - \delta r, 2M + \delta r)$ with $\delta r = M/1000$ and numerically solved the ODE otherwise.	36
4.3	Outgoing radial function. Dashed lines correspond to the real part of the radial function, while continuous lines correspond to the imaginary part. $\alpha = 4iM\sigma$. Here, we used our Fröbenius expansion in the interval $r \in (2M - \delta r, 2M + \delta r)$ with $\delta r = M/1000$ and numerically solved the ODE otherwise.	38
4.4	Upgoing radial function. Dashed lines correspond to the real part of the radial function, while continuous lines correspond to the imaginary part. Here, we used our Fröbenius expansion in the interval $r \in (2M - \delta r, 2M + \delta r)$ with $\delta r = M/1000$ and numerically solved the ODE otherwise.	40

4.5 Comparison between $R_{\ell\omega}^{up}(r)$ and $r\omega R(r)$, where $R(r)$ is given by Eq. 4.44, where we took the expression corresponding to the large ωr -limit $e^{i\omega r}/(2i)^{1+\alpha}\omega r$. Continuous curves represent the functions absolute value of the real part, while dashed lines correspond to absolute imaginary. On the other hand, the green color curves show the large ωr asymptote, while blue ones show upgoing modes – calculated with large r -asymptote. We notice the good agreement between them. 43

4.6 Comparison between $R_{\ell\omega}^{in}(r)$ and $R_{\ell 0}^{in}(r)$. Continuous curves represent the functions' absolute value of the real part, while dashed curves correspond to the absolute imaginary part. The green color curves show the exact solution $R_{\ell 0}^{in}(r)$, which in many cases are not visible for being plotted under the solution for $M\omega = 0.01$. We notice the converging behaviour of the small- ω solutions towards the exact solution for $M\omega = 0$ 45

4.7 Comparison between $R_{\ell\omega}^{up}(r)$ and $R_{\ell 0}^{up}(r)$. Continuous curves represent the functions' absolute value of the real part, while dashed curves correspond to the absolute imaginary part. The green color curves show the exact solution $R_{\ell 0}^{up}(r)$, which in many cases are not visible for being plotted under the solution for $M\omega = 0.01$. We notice the converging behaviour of the small- ω solutions towards the exact solution for $M\omega = 0$ 46

4.8 Check using Eq. 4.47 obtained by Candelas. Green curves correspond to the exact asymptotic expression in the RHS of Eq. 4.47, while blue curves correspond to the LHS of this same equation summed up to $\ell = 60$ 47

5.1 We display, in black, a circular geodesic orbit of radius $r = 6M$ and frequency $\Omega = \sqrt{M/r^3}$. The first four null geodesics that start at point x and re-intersect the orbit to the past of x are displayed in colourful lines. Finally, the dashed black curve represents the photon sphere ($r = 3M$). Image credit: [20]. 54

5.2 Density graphs presenting the logarithm behaviour of real parts for the integrands of Eqs. 3.9 - 3.11 as a function of the frequency, ω , and angular momentum, ℓ . The corresponding graphs for the imaginary parts do not show significant differences, therefore, we omit them from this presentation. Finally, we note that when we consider the folded integrands, g_{\bullet} , all of them produce a similar behaviour to that seen in (a). Therefore, they favour the use of ω -smoothing functions, due to the decay behaviour concentrated around ℓ -axis. Snapshot at $\Delta t = 40M$ 55

5.3 Log-plots showing the behaviour of the absolute value of the integrands (f_b , f_u and f_h) of Eqs. 3.9 - 3.11 as a function of ω . Curves in different colors correspond to different values of ℓ . We note that the folded integrands (g_u and g_h) will behave similarly to what is shown in (a). 56

5.4	Graphs showing the contributions of ingoing and upgoing modes, separately, for the integrands for each state as functions of ω with different curve colors representing different choices of ℓ	57
5.5	Real and imaginary part of Unruh two-point correlation function along a circular geodesic orbit. The peaks occur on the exact spacetime point where null geodesics crossings occur (see Fig 5.1) – this time regime shows the first four of these intersections. The ℓ -sum is performed up to $\ell_{cut} = 60$, patterns shown here do not change significantly with larger ℓ_{cut}	58
5.6	Graphs showing the results for the Boulware Green function. Notice that in (c) the divergences' regions show excellent agreement when comparing both methods.	61

List of Tables

3.1	Modes and Boundary Conditions - Region I of the maximally extended Schwarzschild spacetime.	17
3.2	Modes and Boundary Conditions - Regions I and II of the maximally extended Schwarzschild spacetime.	18
4.1	Modes and Boundary Conditions in IEF- Region I.	34
4.2	Modes and Boundary Conditions in IEF - Regions I and II.	34
A.1	Numerical Tests	65

Chapter 1

Introduction

The study of quantum black holes underwent a boost with Hawking in 1974, when he considered aspects of quantum fields propagating on a black hole spacetime [43]. He found that a quantum state initially empty would develop into an (almost) black-body radiation spectrum. Exploring the consequences of his finding, Hawking pointed out that the quantum radiation emitted at late times of a gravitational collapse into a black hole would be given by a mixed state. This may be explained as part of the field would be irremediably dragged into the event horizon [44; 45].

This result implies a violation of the principle of unitary evolution in Quantum Mechanics, since an initially pure quantum state would evolve into a mixed one. This violation is called Information Paradox and is contested by the AdS/CFT duality. Other works have discussed the incompatibility among concepts underlying the Hawking effect [3; 4; 24]. Also, many proposals to solve the paradox have been put forward [48], although, none has been definitely favoured – see also [47].

While the study of Hawking radiation generated by astrophysical objects should remain a theoretical field in the years to come (see, however, [78]), this effect and others related to Quantum Field Theory on Curved Spacetimes can be studied both in theory and laboratory with the use of analogue models. Proposed for the first time by Unruh [80], analogue black holes are physical models that use properties of wave propagation on matter to simulate features of GR-quantum black holes [83; 84; 86]. In the case of Hawking radiation the spacetime geometry and linearized EFE are substituted by (perfect) fluids and fluid dynamics. Explor-

ing this parallel, some experiments claim to have produced such effect, see, for instance, [8; 56; 76; 81; 89].

In fact, the spatial origins of Hawking radiation is a long-lasting open question. And, although the general belief defends that the phenomenon should be rooted on arbitrarily close distances from the event horizon (giving rise to what is called the Transplanckian problem [12; 51]), authors exploring the parallels between black holes and analogue holes counter-claim that, in fact, the phenomenon seems to arise from smaller frequencies, therefore, not necessarily close to the classical event horizon.

Returning to the theoretical approach, some studies made extensive use of the two-point correlation quantum functions in order to gain better insight into the physics described by them – such as Hawking radiation and the information paradox (e.g., [66; 75]). Nevertheless, they were restricted to toy-model black hole spacetimes. One of our objectives is to build the mathematical and numerical instruments necessary for the calculation of the Feynman two-point correlation function for a scalar field in a four-dimensional Schwarzschild spacetime, with points on opposite sides of the horizon. With this in mind, we explore methods that recently became implementable – such as the MST [74] –, allowing for the analytical calculation of scalar field perturbations both outside and *inside* a Schwarzschild black hole.

We point out that this work may also facilitate the study of black hole’s properties other than the quantum ones. In fact, the study of linear field perturbations (given by mode solutions) of black holes spacetimes is also important for understanding classical properties of these objects. For instance, the classical application of mode solutions includes studies showing that field perturbations across the event horizon lead to instabilities in the interior of certain black holes (see, e.g., [65; 69; 73]).

Jointly, methods to obtain mode solutions of the scalar field equation – outside and inside the event horizon – and the (numerical) implementation of quantum two-point correlation functions (with both points external to the event horizon) give a precise frame of the fabric of our work.

With the aim of studying mode solutions, we have chosen to mostly work with Ingoing Eddington-Finkelstein (IEF) coordinates, as opposed to the more widely used Schwarzschild coordinates. The reason being that IEF coordinates not only render the wave field equation

separable, but also are regular across the future event horizon – as opposed to Schwarzschild coordinates. We also note that separability is a desirable property of the field equation as it facilitates the practical calculation of its solutions and of other quantities, such as the correlations functions that we are interested in.

Indeed, in order to implement the two-point correlation functions with both points in the exterior of the black hole, we use two different approaches to obtain mode solutions: one makes use of series representations, linear combinations and MST coefficients; and another involves numerical integration of differential equations. Given their different natures, they offer useful cross-checks that we explore to help establish the consistency of our results.

This thesis is organized in six chapters. The first and last correspond to Introduction and Conclusions, respectively. Chapter 2 presents an overview of theoretical and observational aspects of General Relativity, particularly black holes. In Chapter 3, we briefly discuss Quantum Field Theory on Curved Spacetimes, focusing on black holes and (quantum) scalar fields. Finally, we present the main results of this thesis in Chapters 4 and 5.

Chapter 4 contains a thorough analysis of the massless scalar field equation on a Schwarzschild background, studying separability, singular points, mode solutions, series representations, and numerical calculation of modes with physically relevant boundary condition. This chapter contains not only results which are already known in the literature, but also new ones – in particular, our proposal to extend upgoing modes across the event horizon with the association of methods by Damour and Ruffini [31] and by Mano, Suzuki and Takasugi (see [74] for a thorough review) and analytical asymptotics/exact mode expressions. The results presented here are also valuable due to our exhaustive testing of independent, but comparable numerical implementations.

In Chapter 5, we discuss the calculation of specific Feynman Green Functions, using numerical ingredients built in the previous chapter. In this chapter, we obtain a general property regarding the real part of these two-point functions and use it as a consistency check of our numerical results. In Section 5.2, we explore this general property in order to compare part of our results against previously-obtained results [20], as graphically demonstrated in a log-plot comparing the divergent structures of the Retarded Green function and the real part of a Feynman Green function. There, we find that the Feynman Green functions follow

the divergence patterns conjectured in [18; 22].

We note that this thesis does not intend to present an exhaustive or complete bibliographic overview of classical black holes, quantum field theory in curved spacetimes or quantum black holes. The reason for such choice relies on the fact that there are many reviews on the topic for a variety of audiences and approaches. In each of the review chapters present here, though, we suggest at least one reference that is both complete and technical and has been recognized by its clarity in exposing the area. Moreover, in the results' chapters, our intent is to contribute to the physical discussion and add a few building blocks to the research on quantum fields on a curved background. We also understand that any progress presented in this text opens up more questions in this field and paves the way to provide a better understanding of them.

Finally, throughout the text, we use the metric signature $(-, +, +, +)$ and geometrized Planck units ($G = 1$, $c = 1$ and $\hbar = 1$). Dimensionful quantities are expressed in terms of the black hole mass, M , and, when the dimensions are not explicitly written out, the results should be understood under the light of the black hole's mass-choice $M = 1$.

Chapter 2

Black Holes

This chapter starts with a review on minimal aspects of General Relativity necessary to study the mathematical objects called black holes and presents an overview of the Schwarzschild spacetime, which is one of the objects of this research. Also, we summarize up-to-date observational evidence for astrophysical black holes.

2.1 Foundations of General Relativity

The discussions presented in this section and in Section 2.2 are based on works by Wald [85], Misner et al [62], Hawking and Ellis [46], and Choquet-Bruhat [27]. Nonetheless, whenever necessary, we use further literature and explicitly refer to it.

Einstein's proposal for a classical theory of Gravity encompasses two main ideas: the Equivalence Principle and Mach's Principle. In General Relativity, the fact that all test particles follow the same path is manifest in them not being pulled by a force, but following a trajectory that extremizes its path. This property also manifests itself in the possibility for the spacetime manifold to be curved, usually forbidding the existence of a global family of inertial observers. In other words, the Equivalence Principle is encompassed by the fact that the spacetime itself carries the gravitational properties and that test particles are obliged to follow geodesics of the manifold. On the other hand, Mach's principle is reflected in the freedom that the spacetime has to adapt itself to its matter and energy contents, being itself the carrier of Gravity.

Einstein's field equations (EFE) are

$$R_{ab} - \frac{1}{2}Rg_{ab} + \Lambda g_{ab} = 8\pi T_{ab}, \quad (2.1)$$

where g_{ab} , R_{ab} , T_{ab} are the metric, Ricci curvature and stress-energy tensors, while R , the trace of R_{ab} , is a curvature scalar and Λ is the cosmological constant – henceforth considered to be null. Eqs. 2.1 are such that they determine the geometry of the spacetime given a certain distribution of matter – while the reverse is also true.

A few words should be said about the stress-energy tensor, which will appear in the discussions to come. Taking into account only continuous distributions of matter, this tensor is written in terms of the spacetime metric and of these distributions and their covariant derivatives. Due to the contracted Bianchi identity, the stress-energy tensor satisfies the local conservation equation

$$\nabla^a T_{ab} = 0. \quad (2.2)$$

Although this tensor encompasses both energy, momentum and stress quantities, as Wald argues [85], Eq. 2.2 can be understood as an approximate conservation relation for the classical notion of energy, whenever considering scales sufficiently small in comparison to the radius of curvature.

Although there are many inequivalent definitions for the stress-energy tensor, we use the Hilbert definition:

$$T_{ab} = -\frac{2}{\sqrt{|g|}} \frac{\delta S_M}{\delta g^{ab}}. \quad (2.3)$$

It involves the functional derivative of S_M , which is the matter component of the action S . This definition guarantees the properties of symmetry and conservation of this tensor.

General Relativity has withstood empirical classical tests - such as the precession of the perihelion of Mercury, bending of a starlight by the Sun and the gravitational redshift of light with the Mösbauer effect. Apart from these verifications, this theory also is in accord with tests of light-travel time-delay (Shapiro delay), frame dragging (Lense-Thirring precession) and null tests with the Post-Newtonian parameters. For a recent and more detailed

discussion, see [91] and references therein. We note that all the tests mentioned so far only probe the weak field limit of General Relativity. As for tests for the strong field regime of this theory, they are significantly less abundant due to the difficulty in performing observations and modelling of strong Gravity field astrophysical environments. One of the available tests is the indirect observation of gravitational waves (the first empirical evidence for the phenomenon) with binary pulsars systems [49; 77]. The most recent test to reaffirm the theory – also probing the strong field regime – has been the direct observation of gravitational waves by Advanced LIGO, which had its best fit given by the modelled merger of two black holes [1?].

2.2 Schwarzschild Black Hole

Schwarzschild spacetime was the first exact solution found to the Einstein’s field equations. This spacetime corresponds to a vacuum solution ($T_{ab} = 0$), yet not to a flat space geometry, but a curved one. This fact, along with a coordinate singularity, the nature of the event horizon and a true gravitational singularity raised the proposal of the so-called “classical observational tests” and criticism. Both, the proposal and the criticism, were essential to the development and establishment of the theory.

This spacetime was obtained from the assumptions of emptiness of matter and energy, spherical symmetry and asymptotic flatness of the Universe. Later, Birkhoff demonstrated that, in fact, this is the unique solution of General Relativity that has these properties. In fact, it is Birkhoff’s theorem along with known interior solutions - other than Schwarzschild’s itself – that gives extreme historical and physical relevance to this solution: the metric describes spherical black holes and the exterior of spherical stars, while it is also a good approximation to slowly rotating stars.

In a few words, Schwarzschild spacetime describes the unique spherically symmetric, asymptotically flat vacuum (black hole) solution of Einstein equations, and these properties are manifest when the metric is written in Schwarzschild coordinates:

$$ds^2 = - \left(1 - \frac{2M}{r}\right) dt^2 + \left(1 - \frac{2M}{r}\right)^{-1} dr^2 + r^2 d\Omega. \quad (2.4)$$

Here, M is the mass of the black hole and $d\Omega = d\theta^2 + \sin^2\theta d\phi^2$; where $r \in (0, \infty)$, in particular, for $r > 2M$ this variable is interpreted as the radial coordinate associated with the circumference; $t \in \mathbb{R}$ is the time as measured by a stationary observer at radial infinity; and $\theta \in [0, \pi]$ and $\phi \in [0, 2\pi)$ are, respectively, polar and azimuthal angles. The event horizon is located at the Schwarzschild radius, $r_{Schw} = 2M$. This coordinate system manifestly becomes irregular at the event horizon.

In this work, we will make extensive use of Ingoing Eddington-Finkelstein (IEF) coordinates. In this coordinate system, the metric is written as

$$ds^2 = - \left(1 - \frac{2M}{r} \right) dv^2 + 2dvdr + r^2 d\Omega, \quad (2.5)$$

where t , θ and ϕ are as in Schwarzschild coordinates, while v is an advanced-time coordinate, and is related to Schwarzschild coordinates by $v = t + r_*$. The tortoise r_* coordinate is given by $r_* = r + 2M \log \left| \frac{r-2M}{2M} \right| \in (-\infty, +\infty)$.

Despite the fact that Schwarzschild coordinates are irregular at $r = 2M$, i.e., both at the past and future event horizons (\mathcal{H}^+ and \mathcal{H}^- , respectively). IEF coordinates are regular throughout regions I and II of the Penrose-Carter diagram, Fig. 2.1 and on the future event horizon \mathcal{H}^+ , which corresponds to the horizon of a black hole formed via spherically-symmetric gravitational collapse. In fact, it is apparent from the equations for radial null geodesics, $dv/dr = 0$ or $dv/dr = 2(1 - 2M/r)^{-1}$, that this coordinate system describes well the infall of massless particles across \mathcal{H}^+ .

For completeness, we also introduce Outgoing Eddington-Finkelstein, Kruskal and Kruskal-Szekeres coordinates. Outgoing Eddington coordinate system gives the metric:

$$ds^2 = - \left(1 - \frac{2M}{r} \right) du^2 - 2dudr + r^2 d\Omega, \quad (2.6)$$

where u is a retarded-time coordinate, and is related to Schwarzschild coordinates by $u = t - r_*$.

Kruskal coordinates' representation of the Schwarzschild spacetime metric is

$$ds^2 = - \frac{r(U, V) e^{\frac{r(U, V)}{2M}}}{8M^3} dUdV + r(U, V)^2 d\Omega, \quad (2.7)$$

where U and V are connected to the advanced and retarded time coordinates u and v through the expressions:

$$U = -e^{-u/4M} \quad (2.8)$$

and

$$V = e^{v/4M}. \quad (2.9)$$

Finally, the metric representation in Kruskal-Szekeres coordinates is given by

$$ds^2 = -32M^3 \frac{e^{-\frac{r(\tau, \chi)}{2M}}}{r(\tau, \chi)} d\tau^2 + 32M^3 \frac{e^{-\frac{r(\tau, \chi)}{2M}}}{r(\tau, \chi)} d\chi^2 + r(\tau, \chi)^2 d\Omega, \quad (2.10)$$

These coordinates produce the Maximally Extended Schwarzschild Spacetime, that is, its geodesics either start/end at a curvature singularity or are ‘‘continuable infinitely with respect to [their] ‘natural length’’ [54]. We show the (compactified) maximal extension of Schwarzschild spacetime in the Penrose-Carter diagram of Fig. 2.1.

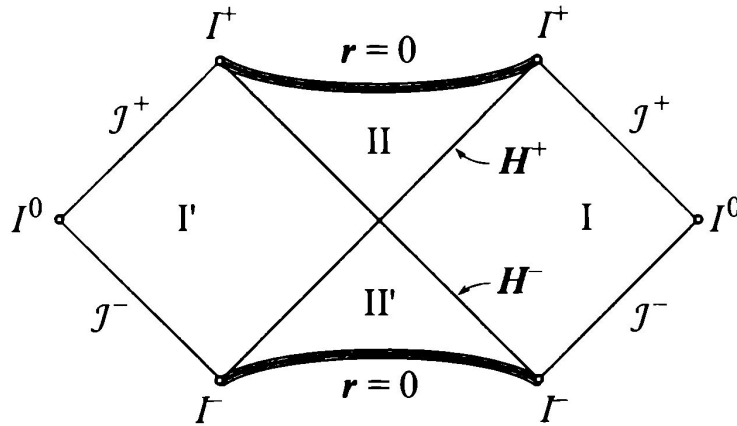


Figure 2.1: Penrose-Carter diagram showing the (compactified) maximal extension of the Schwarzschild manifold. Region II is the black hole interior, II' is the white hole interior, while I and I' are the external regions. \mathcal{H}^+ and \mathcal{H}^- are the future and past event horizons, respectively. \mathcal{J}^+ and \mathcal{J}^- , future and past null infinities. I^+ and I^- are the future and past timelike infinities, while I^0 are the spacelike infinities. Finally, $r = 0$ represent the curvature singularities. A massive particle in region I of a non-eternal Schwarzschild black hole would typically start its trajectory at region I' and either end up at I^+ without entering the black hole or else cross, perhaps, the future event horizon \mathcal{H}^+ entering region II. Image's credit to [39].

Finally, one can relate Kruskal-Szekeres and Schwarzschild coordinate systems by using

the expressions

$$\left(\frac{r}{2M} - 1\right) e^{r/2M} = \chi^2 - \tau^2, \quad (2.11)$$

which is valid for any values of χ and τ , and

$$t = \begin{cases} 4M \tanh^{-1}(\tau/\chi), & \text{in } I \text{ and } II \\ 4M \tanh^{-1}(\chi/\tau), & \text{in } III \text{ and } IV \end{cases}, \quad (2.12)$$

where *I*, *II*, *III* and *IV* are regions of the maximal extension of the Schwarzschild manifold, as shown in Fig. 2.1.

2.3 Observational Evidence for Black Holes

Due to their nature, classical black holes are not detectable per se. Therefore, one needs to consider their interactions with neighbouring matter and radiation. Taking into account absorption effects of matter in its surroundings, the most feasible methods to search for these objects include the search for specific patterns of radio, X-rays and matter jets emissions.

Black hole candidates of masses comparable to that of a star have all been found in binary systems through the detection of X-ray emitted by the gas-accretion from their companion star [23]. These binaries are identified by their outburst patterns, with X-ray emissions increasingly concentrated in time [55]. From theoretical studies, these patterns are only known to be produced either by neutron stars or by black holes; and the identification of the black-hole-nature of the compact object is solely done by the object's mass being larger than the Tolman-Oppenheimer-Volkoff limit – about three solar masses. Examples of these objects are Cyg X-1 (first stellar-mass black holes candidate ever found) [34], MAXI J1659-152 (shortest orbital period) and the companion to the Be-type star MWC 656 [23].

Besides the search techniques outlined here, other methods are used in the study of these objects' nature such as the study of “dying pulse trains” of binary systems expected to host a black hole. These patterns are only possible if the accreting gas around a compact object were to find no surface - therefore, leaving space only for the presence of either an event

horizon or an even more exotic structure [14; 34].

In this direction, scientists have also been investigating matter jets with the Event Horizon Telescope [14; 58] and the Global Millimetre VLBI Array to study AGNs [7], using independent mass-accretion rates measurements to rule out the possibility of a putative surface, as in the study presented at [13] about the nature of the Sgr A*. In fact, the aforementioned observations have respectively also been able to identify structures in the neighbourhood of the Schwarzschild radius and identify the angular size of the jets' source.

Today, the scientific community has strong indications of the existence of black holes, with nearly dozens of objects [52] strongly fitting the characteristics expected to only match either black holes or rather more exotic objects that have been proposed. Finally, the detection of gravitational waves by LIGO offers further indication of the existence of black holes, in special the resulting (final stage) patterns observed agree with those predicted to be produced by (rotating) Kerr black holes. The search to rule out “more exotic objects” continues.

Chapter 3

Quantum Field Theory in Curved Spacetimes

As described by Fewster [35],

“Quantum field theory in curved spacetime [QFT CS] is the study of quantum fields moving in fixed curved spacetime backgrounds. One could think of this as a description of freely falling ‘test quantum fields’, just as geodesics describe the motion of freely falling ‘test particles’: the dynamics of the test system responds to the curvature of spacetime field, but the system does not modify the spacetime itself. So we are ignoring half of Wheeler’s famous slogan that ‘matter tells spacetime how to curve; spacetime tells matter how to move.’”

In this chapter, we aim to present the mathematical and physical machinery necessary to formalize this paragraph: we present a brief review on Quantum Field Theory on Curved Spacetimes following standard literature [10; 35; 37; 38; 39; 40], we explicitly cite other works if otherwise. Also, we discuss some specific results for scalar fields and general features of quantum black holes.

3.1 Linear Approach and Quantum Field Theory in Curved Spacetimes

This section presents an overview of the canonical quantization approach applied to free fields on a curved spacetime background.

We now recall the citation by Fewster in the beginning of this chapter regarding the half ignored slogan on Gravity: the first step adopted in QFT CS is to use perturbation theory up to first order, such that Eqs. 2.1 are reduced to include up to first order matter-field contributions only [25] – as mentioned in Chapter 2, stress-energy tensor associated to a matter field is written only in terms of quadratic terms of field quantities. In other words, when one considers a “faint-enough” field, spacetime decouples from its matter content. Therefore, spacetime is determined by boundary conditions only, while the field will obey a linear wave equation which has the metric as one of its ingredients.

In order to construct a QFT CS, the following ingredients are the most basic ones:

- lagrangian or classical field equation. This also gives origin to a generalized scalar product independent of the Cauchy surface choice, which is essential to establish a complete set of mode solutions of the field equation;
- in the canonical quantization scenario, the quantum field may be expressed in terms of linear combinations of creation and annihilation operators - determined by the choice of mode solutions -, which shall obey appropriate (anti-) commutation relations;
- a vacuum state and its associated Fock space arise from this decomposition.

Nevertheless, the quest for quantization of a field on curved spacetime is not as trivial as the simplification exposed above and, for an overview and discussion of the troubles faced, we refer to [87].

One pivotal difference in relation to flat geometry that troubles this procedure arises from the lack of symmetries on a general curved spacetime. In particular, the absence of Lorentz symmetry interferes with the identification and physical interpretation of quantum states, as in the case of a preferred vacuum quantum state. One materialization of these

difficulties is the ambiguity in the concept of particles [10], which also happens in flat space time for accelerated observers – the particles’ definition is observer-dependent.

Finally, in a second stage, the procedure would be updated to encompass the effects of quantum fields on the spacetime by the modification of EFE to

$$R_{ab} - \frac{1}{2}Rg_{ab} = 8\pi \langle T_{ab} \rangle, \quad (3.1)$$

where $\langle T_{ab} \rangle$ is the renormalized expectation value of the stress energy tensor of the quantum field in a certain quantum state. However, this step has encountered difficulties such as anomalies of the quantized stress-energy tensor (for instance, the conformal anomaly for a conformally invariant massless scalar field) [36].

3.2 Scalar Fields

We now focus our attention to scalar fields, both classical and quantum, and, then, specialize to scalar fields propagating on a Schwarzschild spacetime background.

A scalar field is a field invariant under relevant coordinate transformations of the theory. This spinless field evolves according to the Klein-Gordon (KG) equation. In Minkowski spacetime, this equation has the form

$$\nabla_a \nabla^a \varphi - m^2 \varphi = 0 \quad (3.2)$$

where the $\nabla_a \nabla^a$ operator is given by $\nabla_a \nabla^a = -\partial_t^2 + \partial_x^2 + \partial_y^2 + \partial_z^2$, in rectangular coordinates. The factor m is interpreted as the mass associated to the field.

Following Fewster’s words - “One could think of this as a description of freely falling ‘test quantum fields’ ” - or, more precisely, following the Equivalence Principle, this equation is generalized to

$$\nabla_a \nabla^a \varphi - m^2 \varphi - \xi R \varphi = 0 \quad (3.3)$$

where the D'Alembertian operator is given by

$$\nabla^\mu \nabla_\mu = \frac{1}{\sqrt{|g|}} \partial_\mu \left(\sqrt{|g|} g^{\mu\nu} \partial_\nu \right). \quad (3.4)$$

We recall that g_{ab} is a general spacetime metric, R is the Ricci curvature scalar and m is a mass parameter. Finally, ξ is a coupling constant and this denomination arises from the fact that $\xi = 1/6$ gives rise to a conformally invariant theory - see [85] for a brief, but clear exposition of this topic, comprising the reasons for the presence of the curvature scalar.

The Lagrangian density associated to Eq. 3.3 is given by

$$\mathcal{L} = \partial_a \varphi \partial^a \varphi + m^2 \varphi^2 + \xi R \varphi^2, \quad (3.5)$$

which generates the appropriate wave equation. Moreover, if we fix $\xi = 0$ the above Lagrangian density generates the classical stress-energy tensor

$$T_{ab} = \partial_a \varphi \partial_b \varphi - \frac{1}{2} g_{ab} (\partial_c \varphi \partial^c \varphi + m^2 \varphi^2), \quad (3.6)$$

notice that only quadratic terms appear in it. Finally, the generalized scalar product defined for this field is given by

$$(\varphi_1, \varphi_2) = i \int_\Sigma (\varphi_1^* \partial_a \varphi_2 - \varphi_2 \partial_a \varphi_1^*) d\Sigma^a, \quad (3.7)$$

where Σ is any Cauchy surface, $d\Sigma^a$ is the element of volume and φ_i , $i = 1, 2$ is a scalar field solution. We note that Eq. 3.7 is defined such that the Klein-Gordon equation (Eq. 3.3) and Gauss theorem jointly result in flux conservation through Cauchy surfaces.

We now look into mode decompositions of the scalar field in the specific case of Schwarzschild metric expressed in the coordinate system of same name. While details of mode decomposition will be given in Chapter 4, we present in Tables 3.1 and 3.2 boundary conditions related to KG solutions of the form $\varphi_{\ell\omega m}(t, r, \theta, \phi) = e^{-i\omega t} Y_{\ell m}(\theta, \phi) R_{\ell\omega}(r)/r$, where $Y_{\ell m}$ are spherical harmonics.

We notice that the coefficients A_{in} , A_{out} , B_{in} , B_{out} presented in Tables 3.1 and 3.2 are

Table 3.1: *Modes and Boundary Conditions - Region I of the maximally extended Schwarzschild spacetime.*

Mode	Boundary Conditions
$R_{\ell\omega}^{in}(r) \sim$	$e^{-i\omega r_*}, \quad r_* \rightarrow -\infty$
	$A_{out}e^{i\omega r_*} + A_{in}e^{-i\omega r_*}, \quad r_* \rightarrow \infty$
$R_{\ell\omega}^{up}(r) \sim$	$B_{out}e^{i\omega r_*} + B_{in}e^{-i\omega r_*}, \quad r_* \rightarrow 2M^+$
	$e^{i\omega r_*}, \quad r_* \rightarrow \infty$

called ‘‘radial coefficients’’. They can be obtained exploring the interdependence among these solutions and the Wronskian between $R_{\ell\omega}^{in}(r)$, $R_{\ell\omega}^{in}(r)^*$ and $R_{\ell\omega}^{up}(r)$. Another possibility is to obtain the radial coefficients by means of the MST method¹.

These boundary conditions (Tables 3.1 and 3.2) can be obtained from the asymptotic behaviour of Fr obenius expansions and physical arguments – more details are also given in Chapter 4. The solutions corresponding to Table 3.1 are graphically represented in Fig. 3.1.

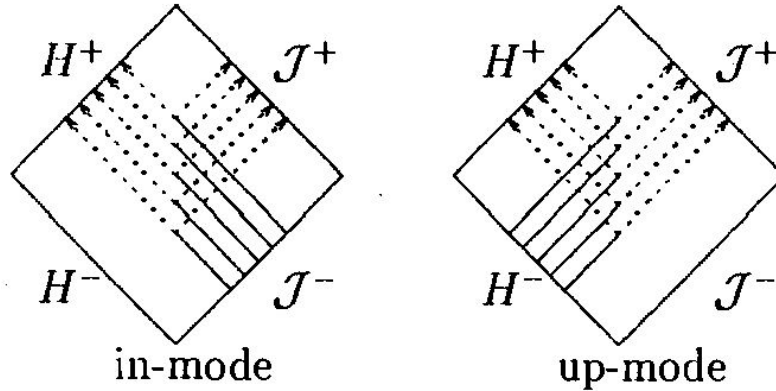


Figure 3.1: *Ingoing and upgoing modes in Region I of a maximally extended Schwarzschild spacetime. Credit to [39].*

Damour and Ruffini were able to extend boundary conditions across the future event horizon with the use of analytical continuation by means of the prescription $r \rightarrow r - i0$ [31; 59]. These results in particular can be seen in Table 3.2².

Finally, we note that the sets of ingoing and outgoing modes are orthonormal with respect to the scalar product defined above, as can be seen from their data on the characteristic

¹As shown in a paper by Sasaki et al [74], ingoing solutions can be represented as a series of hypergeometric functions or a series of Coulomb wave functions, for instance. Due to the unicity of analytical solution and the overlap between convergence regions for these two series representations, the authors obtain a complete analytic solution for this radial solution employing a power-matching process. This process also provides analytical series expressions for the radial coefficients.

²We point out that we fixed here a typo present on Table 2 in [15].

Table 3.2: *Modes and Boundary Conditions - Regions I and II of the maximally extended Schwarzschild spacetime.*

Mode	Boundary Conditions
$R_{\ell\omega}^{in}(r) \sim$	$e^{-i\omega r_*}, \quad r \rightarrow 2M^+$
	$e^{-i\omega r_*}, \quad r \rightarrow 2M^-$
$R_{\ell\omega}^{out}(r) \sim$	$(r - 2M)^{i4M\omega} e^{-i\omega r_*}, \quad r \rightarrow 2M^+$
	$e^{4\pi M\omega} (2M - r)^{i4M\omega} e^{-i\omega r_*}, \quad r \rightarrow 2M^-$

initial data surface given by $\mathcal{J}^- \cup \mathcal{H}^-$. Also, since in- and outgoing modes form a complete set, upgoing modes can be given by linear combinations of this pair of modes – as it will be discussed in Chapter 5.

Returning to the QFT CS discussion, we point out that the relevant vacua and annihilation and creation operators are established by means of physical arguments. For instance, in the case of the Hawking effect, the state that models a black hole emitting Hawking radiation to \mathcal{J}^+ is empty at \mathcal{J}^- . For a scalar field, commutation relations are established as usual once the mode expansion is stated, as discussed in Sec. 3.3.

In Nature, the only experimentally detected field corresponding to a scalar field is the Higgs boson with associated mass of 125 Gev, approximately [26]. Nevertheless, other entities are well-modelled by a scalar field under appropriate regimes – see for instance the case of pions [2] –, even though these are today known to be composite particles. Phonons in a lattice can also be modelled by scalar fields in some instances [70].

Despite the relative phenomenological relevance of the scalar field, the Klein-Gordon equation is extensively studied in both classical and quantum research areas. This fact owes specially to the simplicity of the wave equation when compared to non-zero spin fields, along with similarities in the Physical properties shared among scalar and higher-spin fields – which allows one to draw conclusions that can be extended for other fields, such as the case of the Casimir Effect for fields of spin zero and one in Minkowski spacetime through Hertz potential [30; 63].

Finally, in the classical context, scalar fields are also used as first approach to study the stability of given spacetime solutions of General Relativity or other theories. Starting with the hypothesis of a faint matter distribution, one can study the evolution determined by Eq. 3.3 to verify that the evolved solution continues to obey the faint limit hypothesis - as

a consistency check. Examples include the stability of Schwarzschild and Kerr spacetimes surrounded by this bosonic field [9; 29; 32; 53; 90].

3.3 Semi-Classical Black Holes

The study of quantum black holes underwent a boost with Hawking in 1974, when he considered aspects of quantum fields propagating on a black hole spacetime. Making use of geometric optics and late-time behaviour after the gravitational collapse of the progenitor star, Hawking found that a quantum state that is empty at past null infinity, \mathcal{J}^- , contains quantum radiation at future null infinity, \mathcal{J}^+ . It is important to clarify that it was later proved that his results were robust and not dependent on the geometric optics hypothesis - see [37]. Moreover, it was found that the linear coefficients relating ingoing and outgoing representations (relevant at \mathcal{J}^- and \mathcal{J}^+ , respectively) of this quantum state presented an (almost) black-body radiation spectrum behaviour. Therefore, a temperature could be associated to this black hole induced emission. This temperature was found to be given by

$$T_H = \frac{1}{8\pi M} \approx \frac{6.4 \times 10^{-8}}{M_\odot} \text{K}, \quad (3.8)$$

where M_\odot is the black hole mass, M , expressed in solar mass units.

From the observational point of view, it is relevant to point out that the black holes candidates found in Nature so far have a Hawking temperature orders of magnitude smaller than the CMB's ($\approx 3\text{K}$). Following Parentani and Spindel's reasoning, this implies that - in practice - only massless particles would be emitted through the Hawking radiation process for a black hole which has not reached the latest evaporation stages [67].

We now define Green functions for different quantum states, since this thesis will partly focus on the calculation of this two-point correlation function for a massless scalar field on a Schwarzschild background. We will be considering three different quantum states and their two-point correlation functions³ [16; 61]:

- Boulware vacuum [11]

³The Feynman Green function, G_F , is defined as $iG_F = \Theta(t-t') \langle 0|\phi(x)\phi(x')|0\rangle + \Theta(t'-t) \langle 0|\phi(x')\phi(x)|0\rangle$, where t (t') is the Schwarzschild time associated to the spacetime point x (x'), Θ is the step function and $|0\rangle$ is the vacuum state under consideration (here, Boulware, Unruh and Hartle-Hawking).

It is associated to a cold star and it is obtained from the requirement that normal modes are positive frequency with respect to the timelike Killing vector in the exterior region of the Schwarzschild black hole, $\partial/\partial t$. The Feynman Green function when the field is in the Boulware state is:

$$G_B(x, x') = i \sum_{\ell=0}^{\infty} \sum_{m=-\ell}^{\ell} \int_0^{\infty} \frac{d\omega}{4\pi\omega} (\vec{u}_{\ell\omega m}(x) \vec{u}_{\ell\omega m}^*(x') + \overleftarrow{u}_{\ell\omega m}(x) \overleftarrow{u}_{\ell\omega m}^*(x')), \quad (3.9)$$

where $\vec{u}_{\ell\omega m}(x)$ ($\overleftarrow{u}_{\ell\omega m}(x)$) are mode solutions of the 3+1-dimensional homogeneous KG equation and are determined by upgoing (ingoing) boundary conditions, but taking into account a different normalization – see [16] to relate this normalization to that proposed in Tables 3.1 and 3.2 which is referred to as $\varphi_{\ell\omega m}^{up}$ ($\varphi_{\ell\omega m}^{in}$).

- Unruh vacuum [79]

It is associated to Hawking radiation of an evaporating black hole. One set of modes are required to have positive frequency with respect to the aforementioned Killing vector, while the other independent set of modes should be positive frequency with respect to the U-Kruskal coordinate. The Feynman Green function when the field is in the Unruh state is:

$$G_U(x, x') = i \sum_{\ell=0}^{\infty} \sum_{m=-\ell}^{\ell} \int_{-\infty}^{\infty} \frac{d\omega}{4\pi\omega} \left(\frac{\vec{u}_{\ell\omega m}(x) \vec{u}_{\ell\omega m}^*(x')}{1 - e^{-8\pi M\omega}} + \Theta(\omega) \overleftarrow{u}_{\ell\omega m}(x) \overleftarrow{u}_{\ell\omega m}^*(x') \right), \quad (3.10)$$

where $\Theta(\omega)$ is the heaviside function;

- Hartle-Hawking vacuum [42]

It is interpreted as the state describing a black hole in thermal equilibrium with its own quantum radiation. It is defined by expanding the field in terms of two sets of modes: one set of modes having positive frequency with respect to the U -Kruskal coordinate and the other set having positive frequency with respect to the V -Kruskal coordinate. The Feynman Green function when the field is in the Hartle-Hawking state is:

$$G_H(x, x') = i \sum_{\ell=0}^{\infty} \sum_{m=-\ell}^{\ell} \int_{-\infty}^{\infty} \frac{d\omega}{4\pi\omega} \left(\frac{\vec{u}_{\ell\omega m}(x) \vec{u}_{\ell\omega m}^*(x')}{1 - e^{-8\pi M\omega}} + \frac{\overleftarrow{u}_{\ell\omega m}^*(x) \overleftarrow{u}_{\ell\omega m}(x')}{e^{8\pi M\omega} - 1} \right). \quad (3.11)$$

Exploring the consequences of his findings, Hawking pointed out that the black hole radiation emitted through Hawking’s process would be given by a mixed state, since part of the field would be irremediably dragged into the event horizon [44; 45]. This forecast – along with its contestation (there should be no information loss) by AdS/CFT duality – created the so-called Information Paradox: “throughout the black hole formation and evaporation processes, an initially pure quantum state on \mathcal{J}^{-4} evolves into a mixed quantum state on \mathcal{J}^{+5} , seemingly in violation of the Unitarity Principle of quantum mechanical Physics. The conclusion obtained with black hole duality is indirect, therefore does not offers immediate hints on the Physical problems present on QFT CS leading to this contradiction.

This AdS/CFT conclusion depends, however, on the following assumptions [3; 4]:

- no dramatic effects for a freely falling observer⁶;
- at least order one validity of the QFT CS effective field theory outside the event horizon;
- purity;
- Bekenstein-Hawking entropy defining the density of black hole’s states in its exterior;
- no observer should see any violation of quantum mechanics;

and it is shown that at least one of these hypotheses should fail for the occurrence of Hawking radiation, hinting on the physical issues that a quantum Gravity theory should face in order to be complete and successful. Many proposals to solve the paradox were put forward [48]. Nonetheless, none has been definitely favoured – see also [47]. Other works have also discussed the incompatibility of conceptual sets such as the case of the triad “classical black hole, semi-classical Hawking emission and geometry quantization”, where any pair of these concepts precludes the third [24].

⁴ \mathcal{J}^{-} is a full characteristic initial data surface at early times.

⁵ \mathcal{J}^{+} is a full characteristic initial data surface at late times.

⁶Citing Almheiri et al [3], the “no dramatic effects” should be understood as meaning “both that any low-energy dynamics this observer can probe near his worldline is well-described by familiar Lorentz-invariant effective field theory and also that the probability for an infalling observer to encounter a quantum with energy $E \gg 1/r_s$ (measured in the infalling frame) is suppressed by an exponentially decreasing adiabatic factor as predicted by quantum field theory in curved spacetime.”

Finally, a few words about acoustic black holes are in order. As the name suggests, acoustic/analogue black holes are physical models that use properties of wave propagation on matter to simulate features of GR-quantum black holes. In the case of Hawking radiation, the spacetime geometry and linearized EFE are substituted by (perfect) fluids and fluid dynamics equations, as suggested for the first time by Unruh [80]. We highlight the reasons for the appeal related to these analogue models:

- phonons in perfect fluids presenting a sonic event horizon (see [84]) show a mathematical behaviour similar to Hawking radiation as predicted for quantum fields around black holes;
- the physical phenomena involved are well understood;
- microscopic scales represent a transitioning regime where fluid dynamics stop being valid similarly to what is expected for QFT CS in transplanckian scales [83]. Moreover, the Hawking-radiation-like mathematical behaviour is maintained even when these microscopic scales are explicitly considered under reasonable assumptions [86];
- it is expected that it is possible to create this phenomenon in a laboratory, due to the fact that the corresponding radiation at a laboratory is much easier to be observed than that in astrophysical settings. Although under much debate, some experiments claim to have produced such effect, see, for instance, [8; 56; 76; 81; 89].

3.4 QFT CS: Motivations and Beyond

Quantum Field Theory in Curved Spacetimes is the fact that this theory has a rich and interesting phenomenology - as in the case of Hawking radiation, which, besides its beauty, presents a resilient mathematical structure (see discussion for analogue models above). It is also hoped that the physical and mathematical control that we have over this approach will help us to identify structures that are essential to a quantum theory of gravity - see discussions above involving Lorentz symmetry and, later, Hawking radiation and AdS/CFT for examples of this theoretical/mathematical interplay.

Finally, it should be mentioned that the procedures mentioned here are related to the constructive approach to the theory, which is extremely useful to probe specificities of the theory and related phenomena. Nevertheless, this theory can also be studied through a more mathematical point of view, where the relations between algebraic field structure and spacetime are explored in order to obtain a more general understanding of the features of this theory and its shortcomings – see [5] for omnibus reviews and discussions of Algebraic Quantum Field Theory.

Chapter 4

Wave Equation and Radial Solutions

In this chapter we present and discuss both the analytical and numerical results that we have obtained so far for the Klein-Gordon massless wave equation on a Schwarzschild spacetime. This chapter is organized in five different sections.

The first section refers to the separability and decoupling of the massless scalar field wave equation, which is obtained according to the choice of coordinate representation. The second focuses on the study of the singular points of the radial equations obtained from Eq. 3.3 and the choice of Ingoing (Outgoing) Eddington-Finkelstein coordinates. In Section 4.3, we study series expansions of the radial mode solutions at the regular singular points and radial infinity. Section 4.4 deals with the explicit calculation of ingoing, outgoing and upgoing mode solutions as fixed by Tables 3.1 and 3.2. Finally, we deal with exact and asymptotic radial solutions.

The results presented here are essential for the calculation of the two-point correlation functions presented in the next chapter, Chapter 5. Moreover, they also are a cornerstone for the continuation of this work with the study of correlations across the horizon, since we extend the upgoing modes (defined below in Table 4.1) across the future event horizon.

4.1 Separability of the Wave Equation

In order to obtain solutions of the massless scalar field equation in Schwarzschild spacetime, we derived various coordinate representations for the wave operator and - whenever

possible - showed the separation of this partial differential equation into ordinary differential equations (ODE).

With the use of Eq. 3.4, we obtained these expressions by hand calculation and cross-checked them against those obtained using the X-Act package [60] for Mathematica - a computer algebra program. We also notice that these expressions were previously obtained by other authors [25; 68; 71].

Using the ansatz $\varphi(t, r, \theta, \phi) = T(t) \bar{R}(r) \Theta(\theta) \Phi(\phi) = T(t) R(r) \Theta(\theta) \Phi(\phi) / r$ and considering Schwarzschild coordinates, we have

$$\frac{\nabla_\mu \nabla^\mu \varphi}{\varphi} = \frac{1}{r^2} \left[\frac{\cot(\theta)\Theta' + \Theta''}{\Theta} + \csc^2(\theta) \frac{\Phi''}{\Phi} + \frac{r^3}{2M-r} \frac{T''}{T} + \frac{r(r-2M)\bar{R}'' - 2(M-r)\bar{R}'}{\bar{R}} \right], \quad (4.1)$$

where primed functions represent their derivative in respect to their argument. Notice that Eq. 4.1 results in the following ODEs for the mode solutions, whenever the solution form $T(t) = e^{-i\omega t}$ is considered:

$$\left(1 - \frac{2M}{r}\right) \bar{R}'' + \frac{2}{r} \left(1 - \frac{M}{r}\right) \bar{R}' + \left(\omega^2 \frac{r}{r-2M} - \frac{\lambda}{r^2}\right) \bar{R} = 0, \quad (4.2)$$

$$\frac{\Theta'' + \cot(\theta)\Theta'}{\Theta} + \csc^2(\theta) \frac{\Phi''}{\Phi} = -\lambda \quad (4.3)$$

where $\lambda = \ell(\ell+1)$ is a separation constant. Here, ℓ is interpreted as the angular momentum associated to that wave component, while ω is its frequency. Finally, considering separation constants and physical boundary conditions, one can see that the solution of Eq. 4.3 is given by $\Theta(\theta) \Phi(\phi) = Y_\ell^m(\theta, \phi)$, where Y_ℓ^m is the spherical harmonic of degree ℓ and order m .

With the use of tortoise coordinates, we can re-write Eq. 4.2 as

$$\frac{d^2 R_{\ell\omega}}{dr_*^2} + [\omega^2 - V_\ell(r)] R_{\ell\omega} = 0, \quad (4.4)$$

which is known as Regge-Wheeler equation. Here V_ℓ is an effective potential given by:

$$V_\ell(r) = \left(1 - \frac{2M}{r}\right) \left(\frac{\lambda}{r^2} + \frac{2M}{r^3}\right). \quad (4.5)$$

Using the ansatz $\varphi(v, r, \theta, \phi) = e^{-i\omega v} \frac{\Psi_i(r)}{r} \Theta(\theta) \Phi(\phi)$, we obtain for the Ingoing Eddington-Finkelstein coordinate representation

$$\begin{aligned} \frac{\nabla_\mu \nabla^\mu \varphi}{\varphi} = & \frac{1}{r^2} \left[\frac{\cot(\theta)\Theta' + \Theta''}{\Theta} + \csc^2(\theta) \frac{\Phi''}{\Phi} + \frac{r(r-2M)\Psi_i''}{\Psi_i} \right. \\ & \left. + 2(M - i\omega r^2) \frac{\Psi_i'}{\Psi_i} - \frac{2M}{r} \right]. \end{aligned} \quad (4.6)$$

Similarly, Considering $\varphi(u, r, \theta, \phi) = e^{-i\omega u} \frac{\Psi_o(r)}{r} \Theta(\theta) \Phi(\phi)$ and Outgoing Eddington-Finkelstein coordinates, we obtain

$$\begin{aligned} \frac{\nabla_\mu \nabla^\mu \varphi}{\varphi} = & \frac{1}{r^2} \left[\frac{\cot(\theta)\Theta' + \Theta''}{\Theta} + \csc^2(\theta) \frac{\Phi''}{\Phi} + \frac{r(r-2M)\Psi_o''}{\Psi_o} \right. \\ & \left. + 2(M + i\omega r^2) \frac{\Psi_o'}{\Psi_o} - \frac{2M}{r} \right]. \end{aligned} \quad (4.7)$$

We see that Eqs. 4.6 and 4.7 are separable and the radial equation can be expressed as:

$$\left(1 - \frac{2M}{r}\right) \Psi''_{\ell\omega} + \left(\frac{2M}{r^2} - 2i\sigma\omega\right) \Psi'_{\ell\omega} - \left[\frac{\lambda}{r^2} + \frac{2M}{r^3}\right] \Psi_{\ell\omega} = 0 \quad (4.8)$$

where the radial solution, $\Psi_{\ell\omega}(r)$, depends on the separation constants ℓ and ω and will be written in either Ingoing or Outgoing Eddington-Finkelstein coordinate system according to the following σ -values:

$$\sigma = \begin{cases} 1, & \text{outgoing} \\ -1, & \text{ingoing} \end{cases}. \quad (4.9)$$

The following remark will be useful in the results to come: the radial solutions to the massless Klein-Gordon equation in Schwarzschild and Ingoing Eddington-Finkelstein coordinate systems' representations - $R_{\ell\omega}(r)$ and $\Psi_{\ell\omega}(r)$, respectively - are related by the following expression:

$$R_{\ell\omega}(r) \underset{\sigma=-1}{=} e^{-i\omega r^*} \Psi_{\ell\omega}(r), \quad (4.10)$$

as can be seen by direct substitution into the differential equation Eq. 4.2.

The differential equation, Eq. 3.3 is not obviously separable whenever considering either Kruskal coordinates and the ansatz $\varphi(U, V, \theta, \phi) = H(U, V) \Theta(\theta) \Phi(\phi)$

$$\frac{\nabla_\mu \nabla^\mu \varphi}{\varphi} = -\frac{r e^{\frac{\tau}{2M}}}{8M^3} \frac{\partial_U \partial_V H}{H} + \frac{V \partial_V H + U \partial_U H}{2MrH} + \frac{1}{r^2} \left(\frac{\cot(\theta) \Theta' + \Theta''}{\Theta} + \csc^2(\theta) \frac{\Phi''}{\Phi} \right),$$

where $r = r(U, V)$, or the Kruskal-Szekeres system and $\varphi(\tau, \chi, \theta, \phi) = F(\tau, \chi) \Theta(\theta) \Phi(\phi)$

$$\frac{\nabla_\mu \nabla^\mu \varphi}{\varphi} = -\frac{r e^{\frac{\tau}{2M}}}{32M^3} \frac{\partial_\chi^2 F - \partial_\tau^2 F}{F} + \frac{\chi \partial_\chi H + \tau \partial_\tau F}{2MrF} + \frac{1}{r^2} \left(\frac{\cot(\theta) \Theta' + \Theta''}{\Theta} + \csc^2(\theta) \frac{\Phi''}{\Phi} \right),$$

where $r = r(\chi, \tau)$.

4.2 Singular Structure of the Radial Equation

As we will present here, the in-, out- and upgoing boundary conditions for the radial solutions – given by Tables 3.1 and 3.2 – are imposed at two of the singular points of Eq. 4.8. We aim to extend these conditions away from these singular points to be able to use numerical integration methods. Therefore, we first classify these singular points and, then, obtain Fröbenius expansions around them. This study can also be partially found in the literature [68].

As it is clear from Tables 3.1 and 3.2 – particularly for upgoing modes –, it is useful for our purposes to rewrite the radial equation, Eq. 4.8, in terms of the variable $z = 1/r$. Through this variable transformation, we arrive at

$$z^4 (1 - 2Mz) \tilde{\Psi}''_{\ell\omega} + [2z^3 (1 - 2Mz) - z^2 (2Mz^2 - 2i\sigma\omega)] \tilde{\Psi}'_{\ell\omega} - [\ell(\ell + 1)z^2 + 2Mz^3] \tilde{\Psi}_{\ell\omega} = 0. \quad (4.11)$$

where $\tilde{\Psi}_{\ell\omega} = \Psi_{\ell\omega} \circ z^{-1}$.

We write Eq. 4.8 (4.11) in the standard form obtaining the following expressions:

$$\Psi''_{\ell\omega} + P(r) \Psi'_{\ell\omega} + Q(r) \Psi_{\ell\omega} = 0, \quad (4.12)$$

where

$$P(r) = \frac{1}{r} \left(\frac{2M + 2i\sigma\omega r^2}{r - 2M} \right), \quad (4.13)$$

$$Q(r) = -\frac{1}{r^2} \left[\frac{\ell(\ell+1)r + 2M}{r - 2M} \right] \quad (4.14)$$

and

$$\tilde{\Psi}'' + \tilde{P}(z)\tilde{\Psi}' + \tilde{Q}(z)\tilde{\Psi} = 0, \quad (4.15)$$

and

$$\tilde{P}(z) = \frac{2}{z^2} \left(z - \frac{Mz^2 + i\sigma\omega}{1 - 2Mz} \right), \quad (4.16)$$

$$\tilde{Q}(z) = -\frac{1}{z^2} \frac{\ell(\ell+1) + 2Mz}{1 - 2Mz}. \quad (4.17)$$

As described in Arfken [6], we analyse the limits for the P and Q (\tilde{P} and \tilde{Q}) functions (ω is considered to be a real quantity) in order to determine the singular structure of the radial equation in Eddington-Finkelstein coordinates' representation, Eq. 4.8. The results are summarized as follows

Case $r \rightarrow 0$:

$$\begin{aligned} \lim_{r \rightarrow 0^+} P(r) &= \infty, & \lim_{r \rightarrow 0^+} P(r)r &= -1 \\ \lim_{r \rightarrow 0^+} Q(r) &= \infty, & \lim_{r \rightarrow 0^+} Q(r)r^2 &= 1 \end{aligned}$$

Case $r \rightarrow 2M^\pm$:

$$\begin{aligned} \lim_{r \rightarrow 2M^\pm} P(r) &= \pm\infty, & \lim_{r \rightarrow 2M^\pm} P(r)(r - 2M) &= 1 + 4i\sigma\omega M \\ \lim_{r \rightarrow 2M^\pm} Q(r) &= \mp\infty, & \lim_{r \rightarrow 2M^\pm} Q(r)(r - 2M)^2 &= 0 \end{aligned}$$

Case $r \rightarrow \infty$:

$$\begin{aligned} \lim_{z \rightarrow 0^+} \tilde{P}(z) &= \infty, & \lim_{z \rightarrow 0^+} \tilde{P}(z) z &= \begin{cases} 2, & \text{if } \omega = 0 \\ \infty, & \text{otherwise} \end{cases} \\ \lim_{z \rightarrow 0^+} \tilde{Q}(z) &= \infty, & \lim_{z \rightarrow 0^+} \tilde{Q}(z) z^2 &= \ell(\ell + 1) \end{aligned}$$

In short, we found that $r = 0$ and $r = 2M$ are regular singular points and $r \rightarrow \infty$ is an irregular singular point - except when $\omega = 0$, in this case the singular point at infinity is regular. This is similar to the singular structure of the radial differential equation in Schwarzschild coordinates 4.2.

4.3 Series Expansions

According to Fuch's theorem [6] and our results on the singularity structure of Eq. 4.8, it is possible to obtain Fröbenius' series expansions around $r = 0$ and $r = 2M$. In order to do that, we will use the following expansions, where n-primed functions are the n-th derivatives of the function with respect to $(r - r_0)$:

$$\Psi_{\ell\omega}(r) = \sum_{n=0}^{\infty} a_n(\ell, \omega) (r - r_0)^{n+\alpha}, \quad (4.18)$$

$$\Psi'_{\ell\omega}(r) = \sum_{n=0}^{\infty} (n + \alpha) a_n(\ell, \omega) (r - r_0)^{n+\alpha-1}, \quad (4.19)$$

$$\Psi''_{\ell\omega}(r) = \sum_{n=0}^{\infty} (n + \alpha)(n + \alpha - 1) a_n(\ell, \omega) (r - r_0)^{n+\alpha-2}. \quad (4.20)$$

where α is an exponent that differentiates between the two independent solutions of the second order differential equation. Inserting Eqs. 4.18 - 4.20 into Eq. 4.8, we obtained the expansions around $r_0 = 0$, $r_0 = 2M$ and $r_0^{-1} \rightarrow 0^+$. We point out that the expansion around infinity ($r_0^{-1} \rightarrow 0^+$) is not covered by Fuch's theorem, therefore we do not expect it to have a non-zero radius of convergence. Despite that, the expansion is useful to understand the asymptotic behaviour of the mode solution.

As already mentioned, we are considering $\lambda = \ell(\ell + 1)$. Also, we henceforth omit the explicit dependence on (ℓ, ω) of the Fröbenius expansion's coefficients, that is, $a_n(\ell, \omega) \mapsto a_n$.

Case $r_0 = 0$:

We have that

$$\begin{aligned}
0 &= \left(1 - \frac{2M}{r}\right) \Psi''_{\ell\omega} + \frac{1}{r^2} (2M - 2i\sigma\omega r^2) \Psi'_{\ell\omega} - \frac{1}{r^2} \left(\lambda + \frac{2M}{r}\right) \Psi_{\ell\omega} \\
&= \left\{ \sum_{m=-2}^{\infty} -2M [(m + \alpha + 2)(m + \alpha) + 1] a_{m+2} r^m + \sum_{m=-1}^{\infty} [(m + \alpha)(m + \alpha + 1) - \lambda] a_{m+1} r^m \right. \\
&\quad \left. - \sum_{m=0}^{\infty} 2i\sigma\omega (m + \alpha) a_m r^m \right\} r^{\alpha-1} \\
\Rightarrow 0 &= \sum_{m=0}^{\infty} \left\{ -2M [(m + \alpha + 2)(m + \alpha) + 1] a_{m+2} + [(m + \alpha)(m + \alpha + 1) - \lambda] a_{m+1} \right. \\
&\quad \left. - 2i\sigma\omega (m + \alpha) \right\} r^m - 2M (\alpha - 1)^2 \frac{a_0}{r^2} + \left\{ -2M \alpha^2 a_1 + [\alpha(\alpha - 1) - \lambda] a_0 \right\} \frac{1}{r}.
\end{aligned}$$

Therefore, we conclude that $\alpha = 1$ and make use of this relation to obtain

$$a_1 = -\frac{\lambda}{2M} a_0, \quad (4.21)$$

$$a_{m+2} = \frac{(m+1)(m+2) - \lambda}{2M(m+2)^2} a_{m+1} - \frac{2i\sigma\omega(m+1)}{2M(m+2)^2} a_m, \quad \forall m \geq 0. \quad (4.22)$$

This results in the first radial solution, $\Psi_{\ell\omega}^{[1]}$, being given by

$$\Psi_{\ell\omega}^{[1]}(r) = \sum_{n=0}^{\infty} a_n r^{n+1}. \quad (4.23)$$

The second solution, $\Psi_{\ell\omega}^{[2]}$, is given by [6]

$$\Psi_{\ell\omega}^{[2]}(r) = \log(r/2M) \Psi_{\ell\omega}^{[1]} + \sum_{n=0}^{\infty} b_n r^{n+1}, \quad (4.24)$$

where b_n are such that $\Psi_{\ell\omega}^{[2]}$ is solution to Eq. 4.8. Therefore, the second solution presents a divergent behaviour as $r \rightarrow \infty$.

Case $r_0 = 2M$:

After the necessary algebra, we have that

$$\alpha = \begin{cases} 0 \\ -4i\sigma M\omega \end{cases} \quad (4.25)$$

For $\alpha = 0$, we obtain the coefficients

$$a_0 = 1 \quad (4.26)$$

$$a_1 = \frac{1 + \lambda}{2M(1 + 4i\sigma M\omega)} a_0 \quad (4.27)$$

$$a_2 = \frac{1}{16M^2(1 + 2i\sigma M\omega)} [\lambda(a_0 + 2Ma_1) - 24i\sigma M^2\omega a_1] \quad (4.28)$$

$$a_n = \frac{-1}{4M^2n(n + 4iM\sigma\omega)} \left\{ 2M [5 + 7(n - 3) + 2(n - 3)^2 - \lambda + 12iM\sigma\omega(n - 1)] a_{n-1} \right. \\ \left. + [(n - 3)^2 + n - 3 - \lambda + 12iM\sigma\omega(n - 2)] a_{n-2} + 2i(n - 3)\sigma\omega a_{n-3} \right\}. \quad (4.29)$$

Similarly, for $\alpha = -4i\sigma M\omega$, we obtain

$$a_0 = 1 \quad (4.30)$$

$$a_1 = \frac{1 + \lambda - 4i\sigma M\omega - 16\sigma^2 M^2\omega^2}{2M(1 - 4i\sigma M\omega)} a_0 \quad (4.31)$$

$$a_2 = \frac{1}{16M^2(1 - 2i\sigma M\omega)} \left\{ \lambda(a_0 + 2Ma_1) + 4i\sigma M\omega [(8i\sigma M\omega - 1)a_0 + 8i\sigma M^2\omega a_1] \right\} \quad (4.32)$$

$$a_n = \frac{-1}{4M^2n(n - 4iM\sigma\omega)} \left\{ -2M [-5 + (4i\sigma M\omega - 7)(n - 3) - 2(n - 3)^2 + \lambda \right. \\ \left. + 4iM\sigma\omega - 16\sigma^2 M^2\omega^2] a_{n-1} + [(n - 3)^2 + (1 + 4i\sigma M\omega)(n - 3) - \lambda + 8iM\sigma\omega \right. \\ \left. \times (1 - 4i\sigma M\omega)] a_{n-2} + 2i(n - 3 - 4i\sigma M\omega)\sigma\omega a_{n-3} \right\}. \quad (4.33)$$

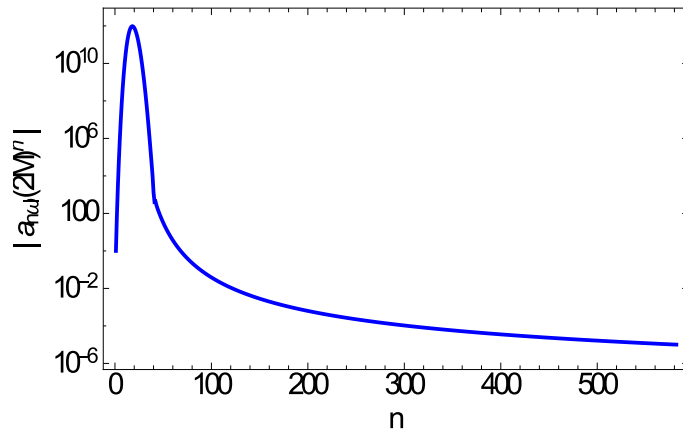


Figure 4.1: Plots of the dimensionless Fröbenius coefficients for the $\alpha = 0$, $\sigma = -1$, $\omega = 1.42618/M$.

Fig. 4.1 indicates that the $\alpha = 0$ coefficients have a strong decay, as expected from Fuch's Theorem, and that the most relevant contribution to the series is concentrated around small values of n . This behaviour is persistent among the various values of ω and ℓ tested. Completely similar behavior is seen for the series' coefficients for $\alpha = -4i\sigma M\omega$.

Case $r \rightarrow \infty$

In this case, we choose to work with expansions of the form

$$\begin{aligned}\Psi_{\ell\omega}(r) &= e^{\beta r} \sum_{n=0}^{\infty} a_n r^{\alpha-n}, \\ \Psi'_{\ell\omega}(r) &= e^{\beta r} \sum_{n=0}^{\infty} [\beta a_n r^{-n+\alpha} + (\alpha - n) a_n r^{\alpha-n-1}], \\ \Psi''_{\ell\omega}(r) &= e^{\beta r} \sum_{n=0}^{\infty} [\beta^2 a_n r^{-n+\alpha} + 2\beta(\alpha - n) a_n r^{-n+\alpha-1} + (\alpha - n)(\alpha - n - 1) a_n r^{\alpha-n-2}],\end{aligned}$$

which results in the pair

$$\begin{cases} \alpha = 0 & , & \beta = 0 \\ \alpha = 4i\sigma M\omega \underset{\sigma=-1}{=} -4iM\omega & , & \beta = -2i\sigma\omega \underset{\sigma=-1}{=} 2i\omega \end{cases} . \quad (4.34)$$

Notice again that, that since this expansion was done at an irregular singular point, this series is not expected to converge.

4.4 Calculation of In-, Out- and Upgoing Modes

In this section, we explicitly discuss the construction of in-, out- and upgoing modes and the different methods used to calculate their associated radial solutions. To facilitate our discussion, it is useful to rewrite Tables 3.1 and 3.2 in Ingoing Eddington-Finkelstein coordinates with the use of Eq. 4.10. The result is given in Tables 4.1 and 4.2.

All graphs presented in this section correspond to the choice of parameters $\omega \approx 0.0070/M$ and $\ell = 2$. α is chosen accordingly to the mode in consideration and $\sigma = -1$, since we are working with IEF coordinates.

As already mentioned in the previous section, we carried out a Fröbenius expansion about

Table 4.1: *Modes and Boundary Conditions in IEF- Region I.*

Mode	Boundary Conditions	
$\Psi_{\ell\omega}^{in}(r) \sim$	1,	$r_* \rightarrow -\infty$
	$A_{out}e^{2i\omega r_*} + A_{in}$,	$r_* \rightarrow \infty$
$\Psi_{\ell\omega}^{up}(r) \sim$	$B_{out}e^{2i\omega r_*} + B_{in}$,	$r_* \rightarrow -\infty$
	$e^{2i\omega r_*}$,	$r_* \rightarrow \infty$

Table 4.2: *Modes and Boundary Conditions in IEF - Regions I and II.*

Mode	Boundary Conditions	
$\Psi_{\ell\omega}^{in}(r) \sim$	1,	$r \rightarrow 2M^+$
	1,	$r \rightarrow 2M^-$
$\Psi_{\ell\omega}^{out}(r) \sim$	$(r - 2M)^{i4M\omega}$,	$r \rightarrow 2M^+$
	$e^{4\pi M\omega}(2M - r)^{i4M\omega}$,	$r \rightarrow 2M^-$

$r = 2M$, thus obtaining two series of the form

$$\Psi_{\ell\omega}(r) = \sum_{n=0}^{\infty} a_n(\ell, \omega) (r - 2M)^{n+\alpha}, \quad (4.35)$$

where $\alpha = 0$ or $-4\sigma iM\omega$, and $a_n(\ell, \omega)$ are coefficients obtained through the use of this series in Eq. 4.8 . It is clear now, from Tab. 4.1, that $\alpha = 0$ corresponds to ingoing modes and $\alpha = 4iM\omega$ to outgoing modes – here and henceforth, we fix $\sigma = -1$, therefore also fixing the use of Ingoing Eddington-Finkelstein coordinates.

Also, one can prove from Eq. 4.2 and Table 3.1 that $R_{\ell\omega}^{in}(r) = e^{-4M\omega i}(2M)^{4M\omega i} (R_{\ell\omega}^{out}(r))^*$ in the interior region – here, $\varphi_{\ell\omega m}^{\bullet}(r) = e^{-i\omega t} R_{\ell\omega}^{\bullet}(r) Y_{\ell m}(\theta, \phi)/r$, with $\bullet = \{in, out, up\}$.

$$\lim_{r \rightarrow 0^+} |\varphi_{\ell\omega}^{\bullet}(r)| = \infty, \quad (4.36)$$

where \bullet now attends to the “in” and “out” labels. This conclusion is reached by the following reasoning:

- in- and outgoing modes form a complete set of solutions for a given ℓ, ω pair;
- their Fröbenius expansions at $r = 2M$ overlap with the Fröbenius expansions at $r = 0$ given by $\Psi_{\ell\omega}^{[1]}$ and $\Psi_{\ell\omega}^{[2]}$;
- Therefore, either in- or out- has the divergent behaviour at $r = 0$ given by the solution $\Psi_{\ell\omega}^{[2]}$ or both present the divergent behaviour, since written as a combination of $\Psi_{\ell\omega}^{[1]}$

and $\Psi_{\ell\omega}^{[2]}$ Fröbenius expansions around zero;

- Nevertheless, we argued that $\varphi_{\ell\omega}^{in}(r)$ and $\varphi_{\ell\omega}^{out}(r)$ are related by complex conjugation. Therefore, among the options above, what remains is that both in- and outgoing modes will be divergent on the spacetime singularity, $r = 0$.

Finally, we note that the β -exponents obtained in Eq. 4.34 reproduce the correct asymptotic behaviour at radial infinity for the in- and upgoing modes - as well for outgoing ones.

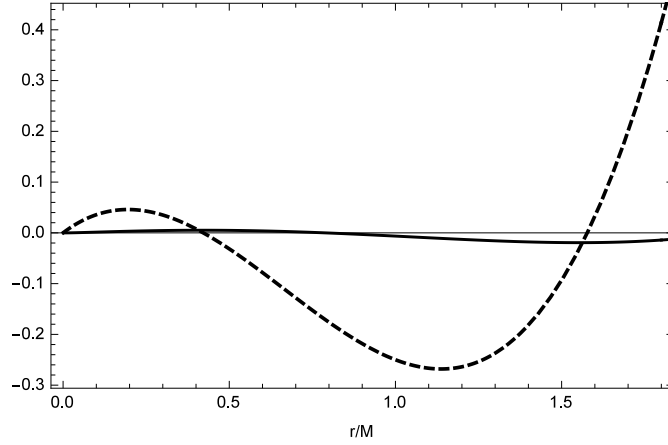
4.4.1 Ingoing modes

In the above discussion, we argued that the $\alpha = 0$ solution of Eq. 4.25 corresponds to ingoing modes in the exterior region of the black hole spacetime. We also showed that the mode $\varphi_{\ell\omega}^{in}(r)$ is divergent at the spacetime singularity. (This divergence is not seen in Fig. 4.2, since we do not integrate until $r = 0$. Also, this divergence is explicit in this interval choice if we consider the ratio between this solution and r .)

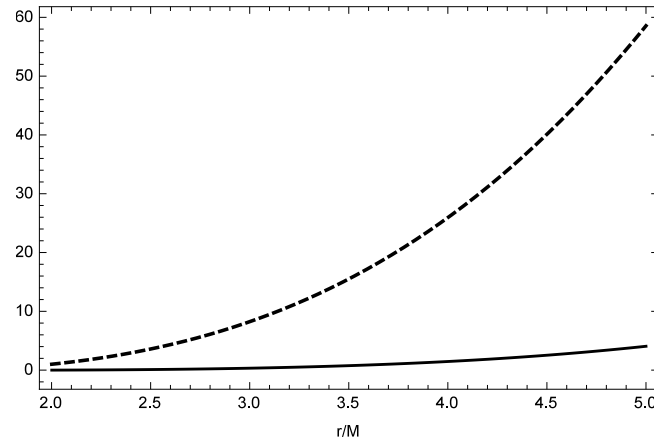
Regarding the ingoing modes, we note that we used three different approaches to calculate them:

- Fröbenius expansion in the open ball $r \in (0, 4M)$;
- Jaffé series, which consists of a series convergent for any value of r larger than $2M$ and well established in the literature [19; 57] - for details on its implementation see references just cited;
- Numerical integration of the differential equation Eq. 4.8 with the use of Eq. 4.35 to set appropriate boundary conditions.

We have used each method accordingly to its convergence rate in a given region. Briefly, Fröbenius is numerically robust in the range $(0, 4M)$, Jaffé is used throughout for $r > 2M$ and numerical integration is used in cases where either ℓ and/or $M\omega$ are large, as well as when we have $r/2M \gg 1$. Nevertheless, despite these characteristic ranges, we also used these different methods to perform cross-checks in the domains' intersections. A compilation of these numerical tests is presented in Appendix A.



(a) Ingoing radial function, $\Psi_{\ell\omega}^{in}(r)M$, in the interior region of Schwarzschild spacetime.



(b) Ingoing radial function, $\Psi_{\ell\omega}^{in}(r)M$, in the exterior region of Schwarzschild spacetime.

Figure 4.2: *Ingoing radial function. Dashed lines correspond to the real part of the radial function, while continuous lines correspond to the imaginary part. $\alpha = 0$. Here, we used our Fröbenius expansion in the interval $r \in (2M - \delta r, 2M + \delta r)$ with $\delta r = M/1000$ and numerically solved the ODE otherwise.*

In Fig. 4.2, we see an example of ingoing radial solution both in the interior and exterior regions of the Schwarzschild black hole. In this particular case, the graph shows a collage of results: the immediate neighbourhood of the event horizon, $r \in (2M - \delta r, 2M + \delta r)$ with $\delta r = M/1000$, is obtained with the Fröbenius series, while the remaining solution is obtained by numerically solving the differential equation with the solutions at $r = 2M \pm \delta r$ as boundary conditions and making use of the Mathematica's command *NDSolve*.

4.4.2 Outgoing modes

We have recognized in the above discussion that the $\alpha = 4iM\omega$ solution of Eq. 4.25 corresponds to outgoing modes. The validity of this expression, however, is limited to the exterior region of the black hole spacetime, as can be seen from Table 4.2.

Therefore, we obtain the internal solution following the prescription by Damour and Ruffini [31; 59] to analytically continue the outgoing solution across the event horizon. Therefore, the implementation of an outgoing mode is given by the following radial solution:

$$\Psi_{\ell\omega}^{out}(r) = \begin{cases} (r - 2M)^{4iM\omega} \sum_{n=0}^{\infty} a_n (r - 2M)^n, & \text{if } 2M < r < 4M \\ e^{4\pi M\omega} (2M - r)^{4iM\omega} \sum_{n=0}^{\infty} a_n (2M - r)^n, & \text{if } 0 < r < 2M \end{cases}. \quad (4.37)$$

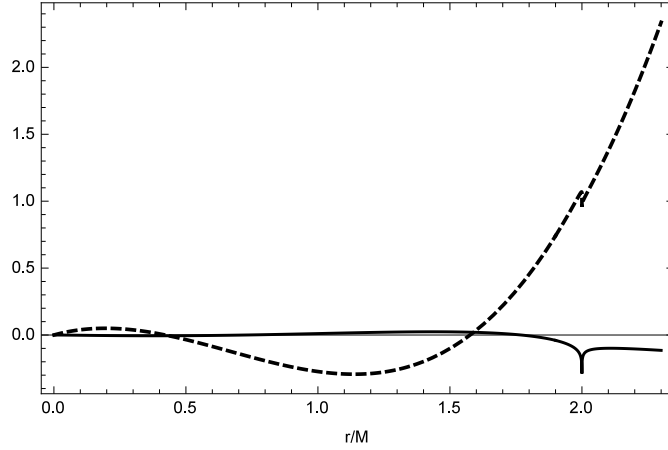
Similarly to the ingoing modes, the outgoing solutions were obtained with the use of the above Fröbenius series, Eq. 4.37, and numerical integration of differential equations. Moreover, this solution is also obtainable from the complex conjugation of the ingoing solution. We note that the method choice is in complete analogy to that described for ingoing modes. Once more, we use these different methods to perform consistency checks shown in Appendix A.

In Fig. 4.3, we present a radial outgoing solution, $\Psi_i(r)$, for the interval $r \in (0, 5M)$, which was again obtained with a collage of the Fröbenius and numerical integration methods.

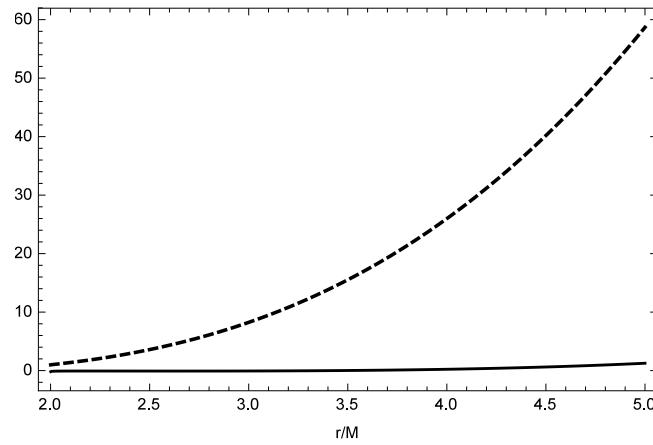
4.4.3 Upgoing modes

In short, upgoing modes were effectively obtained through:

- The use of an asymptotic ansatz (to be introduced);
- Numerical integration, with boundary condition set away from the singular point at radial infinity (i.e., for a large, but finite value of r) with the use of the aforementioned asymptotic form;
- Use of Eq. 4.38 (to be introduced) and of MST coefficients to obtain these modes in the (exterior **and** interior) neighbourhood of the event horizon.



(a) Outgoing radial function, $\Psi_{\ell\omega}^{out}(r)M$, in the interior region of Schwarzschild spacetime.



(b) Outgoing radial function, $\Psi_{\ell\omega}^{out}(r)M$, in the exterior region of Schwarzschild spacetime.

Figure 4.3: *Outgoing radial function. Dashed lines correspond to the real part of the radial function, while continuous lines correspond to the imaginary part. $\alpha = 4iM\sigma$. Here, we used our Fröbenius expansion in the interval $r \in (2M - \delta r, 2M + \delta r)$ with $\delta r = M/1000$ and numerically solved the ODE otherwise.*

As it will become clear in Chapter 5, in our work related to the correlation functions, we either numerically solve the ODE or make use of the asymptotic form aforementioned to calculate upgoing modes. We now discuss in detail these methods, regions of applicability and difficulties that we faced in the numerical implementation of upgoing modes.

Upgoing modes have boundary conditions set at $r \rightarrow \infty$. As already mentioned, the Fröbenius method is not applicable there due to the irregularity of this singular point. Therefore, we consider an Ansatz of the form $\Psi_{\ell\omega}(r) = e^{2i\omega r_* - \mathcal{V}(r)}$ and require that $\mathcal{V}(r) \rightarrow 0$ as $r \rightarrow \infty$. It is straight-forward to obtain an expansion of $\mathcal{V}(r)$ at $r \rightarrow \infty$ up to an appropriate order. This expansion was used, for example, to set the boundary conditions

away from $r = \infty$ in order to numerically solve Eq. 4.8.

Aiming at the construction of our second method for the calculation of upgoing modes, we recall that it is always possible to write upgoing radial solutions as linear combinations of in- and outgoing ones due to the second order linear nature of Eq. 4.8. In fact, using Eq. 4.2 and boundary conditions, we find that

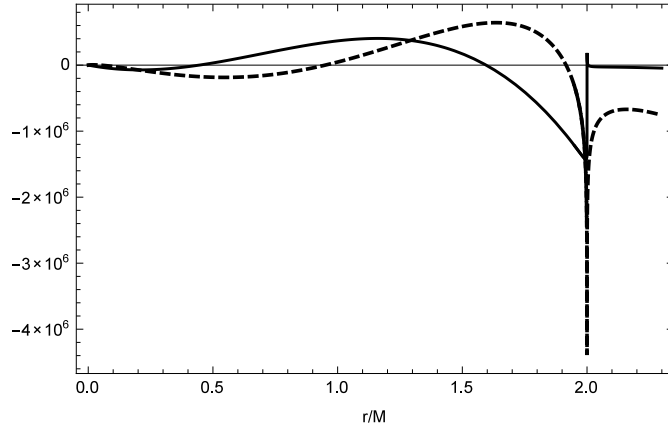
$$R_{\ell\omega}^{up} = -\frac{1}{2i\omega} W_{Schw} (R_{\ell\omega}^{out}, R_{\ell\omega}^{up}) R_{\ell\omega}^{in} + \frac{1}{2i\omega} W_{Schw} (R_{\ell\omega}^{in}, R_{\ell\omega}^{up}) R_{\ell\omega}^{out}, \quad (4.38)$$

where $W_{Schw}(\bullet, \bullet)$ is the Wronskian between two solutions of the radial equation Eq. 4.2 expressed in tortoise coordinate, r_* . Moreover, it is easily shown from this same equation that the Wronskian is constant for any value of r_* . We recall that Eq. 4.10 relates $R_{\ell\omega}^{up}$ and $\Psi_{\ell\omega}^{up}$.

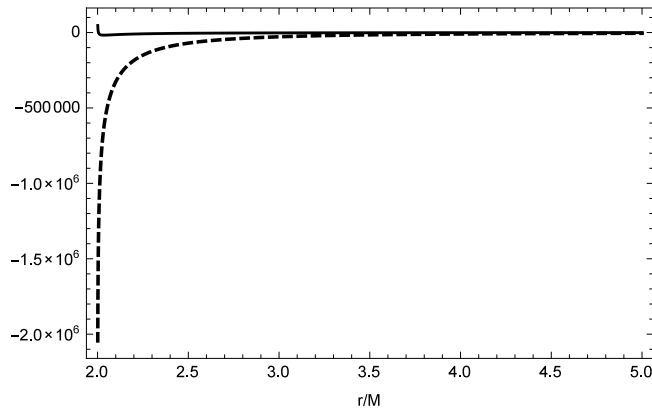
In fact, the relation given in Eqs. 4.38 and 4.8 and the constancy of the Wronskians are extremely useful in our extension of the upgoing solutions across the event horizon: These equations allow us to extend the upgoing modes through the use of the Damour-Ruffini prescription for an analytical continuation across the future event horizon – which was previously only applied to the outgoing modes in Eq. 4.37 – [15]. In practice, we implemented this idea by requiring the coefficients in the linear combination to be fixed even across the horizon, while their determination was done in the exterior region with Eq. 4.38.

A graphical example with a result of this procedure can be seen in Fig. 4.4, where Fig. 4.4(a) was obtained with numerical integration, while Fig. 4.4(b) uses a collage of numerical integration in the exterior region and our application of the Damour-Ruffini method in the interior – here, Wronskians were obtained from the simultaneous solution of the trio of in-, out- and upgoing solutions. Notice that the upgoing radial solution is bounded even across the event horizon.

An important detail should be added at this point: the direct numerical determination of the Wronskian between radial solutions of Eq. 4.2 can be rather tricky: in certain cases it may involve deviations from the correct constant value – as described in detail in papers such as [19]. To find a way around such problem and obtain radial coefficients (linear coefficients in Eq. 4.38), we have successfully used the Mano-Suzuki-Takasugi (MST) method [21; 74].



(a) Upgoing radial function, $\Psi_{\ell\omega}^{up}(r)M$, in the interior region of Schwarzschild spacetime.



(b) Upgoing radial function, $\Psi_{\ell\omega}^{up}(r)M$, in the exterior region of Schwarzschild spacetime.

Figure 4.4: *Upgoing radial function. Dashed lines correspond to the real part of the radial function, while continuous lines correspond to the imaginary part. Here, we used our Fröbenius expansion in the interval $r \in (2M - \delta r, 2M + \delta r)$ with $\delta r = M/1000$ and numerically solved the ODE otherwise.*

In fact, the MST coefficients were also used to determine normalization coefficients required in the calculations of the two-point correlation functions.

We also used another method to obtain such radial coefficients: we simultaneously numerically integrated two copies of Eq. 4.8 subject to ingoing and upgoing boundary conditions [15]. In this case, we avoided the aforementioned deviation problems. However, since the computational cost is high in this second approach, we left it as a “stable” curiosity and made extensive use of the MST method to obtain such coefficients.

Returning to the discussion on methods for the calculation of upgoing modes, we have encountered difficulties with the implementation of Eq. 4.38 in a few random cases due to the fact that the terms of this sum occasionally had similar magnitude and opposite sign, resulting in delicate cancellations and accuracy loss. The work to overcome such problem is

still in progress and is essential to a successful obtainment of upgoing modes. We stress that these two regimes for upgoing modes are essential to the study of the two-point correlation functions – particularly when considering points across the event horizon.

We emphasize that the numerical integration method is more stable than the use of Eq. 4.38 – therefore, we use it in our two-point correlation case-study. Nevertheless, it is computationally expensive to obtain solutions on the exterior neighbourhood of the event horizon through this method, since it involves integrating across at least four orders of magnitude. On the other hand, while the method involving Eq. 4.38, MST and in/outgoing modes is promising, it needs further development regarding the aforementioned numerical cancellations.

4.5 Asymptotics

In this section, we study asymptotic solutions of Eq. 4.8. Doing so, we are able to better understand the asymptotic behaviour of the radial solutions and extend our tests of the mode solutions. These asymptotics may also be directly used in the calculation of the two-point functions. Here, in order to facilitate comparisons against results in the literature, we will use Eq. 4.10 relating radial solutions in Schwarzschild and Ingoing Eddington-Finkelstein coordinate systems.

4.5.1 Large ωr

Here, we followed a procedure adopted for the study of mode solutions in the large ωr limit presented by Creek et al in a higher-dimensional (brane-bulk) scenario [28]. We, however, obtained different results, because we follow what is described in the DLMF encyclopedia as “numerically satisfactory solutions” to the Kummer equation, in the relevant asymptotic limit [33].

We rewrite Eq. 4.2 as

$$\frac{1}{\omega^2} \left[\left(1 - \frac{2M\omega}{r\omega} \right) \bar{R}'' + \frac{2}{r} \left(1 - \frac{M\omega}{r\omega} \right) \bar{R}' + \left(\omega^2 \frac{r\omega}{r\omega - 2M\omega} - \frac{\lambda}{r^2} \right) \bar{R} \right] = 0, \quad (4.39)$$

and make the variable transformation $h(r) = \omega r$ and take the leading order contributions for large h

$$\frac{d^2 \bar{R}}{dh^2} + \frac{2}{h} \frac{d\bar{R}}{dh} + \left(1 - \frac{\lambda}{h^2}\right) \bar{R} = 0. \quad (4.40)$$

We consider the following transformations, where γ is a parameter yet to be determined

$$\begin{aligned} \bar{R}(r) &= e^{-ih(r)} h(r)^\gamma y(h(r)), \\ \bar{R}'(r) &= e^{-ih(r)} z(r)^\gamma \left[\left(\frac{\gamma}{h(r)} - i \right) y(h(r)) + y' \circ h(r) \right], \\ \bar{R}''(r) &= e^{-ih(r)} h(r)^\gamma \left\{ \left[\left(\frac{\gamma}{h(r)} - i \right)^2 - \frac{\gamma\omega}{h(r)^2} \right] y \circ h(r) + \left(\frac{\gamma}{h(r)} - i \right) y' \circ h(r) + y'' \circ z(r) \right\} \end{aligned}$$

which, substituted into Eq. 4.40, result in

$$0 = e^{-ih} h^{\gamma-1} \left\{ h \frac{d^2 y}{dh^2} + 2(1 - ih + \gamma) \frac{dy}{dh} + \left[\frac{(1 + \gamma)(\gamma - 2ih) - \lambda}{h} \right] y \right\}. \quad (4.41)$$

For convenience, once more we changed coordinates to $w = 2iz = 2i\omega r$, in order to obtain the following asymptotic equation for large h :

$$w \frac{d^2 y}{dw^2} + [2(1 + \gamma) - w] \frac{dy}{dw} - \left[1 + \gamma + \frac{\lambda - \gamma(\gamma + 1)}{w} \right] y = 0. \quad (4.42)$$

We notice that this ODE has the same structure as the Kummer's equation [33], when we choose $\gamma \equiv \gamma_\pm = \pm(\ell + \delta_{-, \pm})$, where $\delta_{\bullet, \bullet}$ is the Kronecker delta.

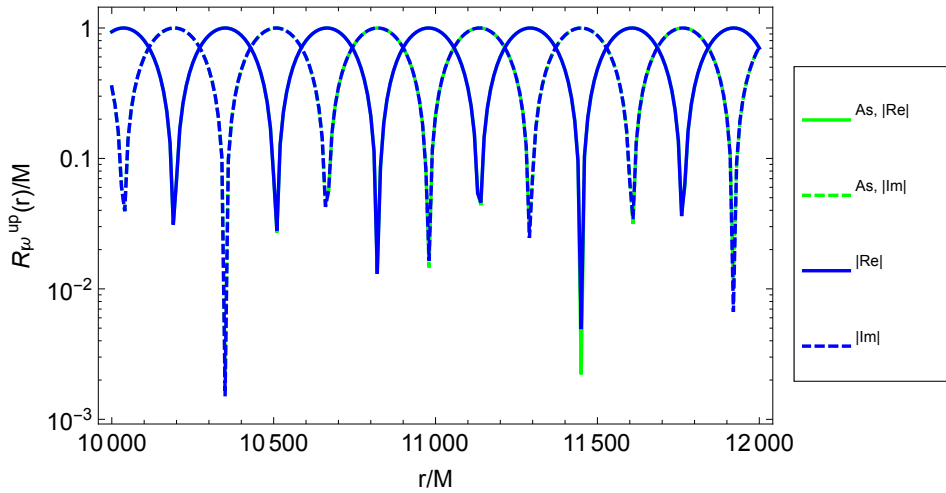
For large values of z , we have that the two ‘‘acceptable solutions’’ to the ODE in this regime are, according to [33],

$$y(z) = \begin{cases} U(1 + \gamma, 2(1 + \gamma), 2iz) & \sim (2iz)^{-1-\gamma} \\ e^{2iz} U(1 + \gamma, 2(1 + \gamma), 2iz) & \sim e^{2iz} (2iz)^{-1-\gamma} \end{cases}, \quad (4.43)$$

which we re-express in terms of the solution of Eq. 4.2:

$$\bar{R}(r) = \begin{cases} e^{-i\omega r} (\omega r)^\gamma U(1 + \gamma, 2(1 + \gamma), 2i\omega r) & \sim \frac{1}{(2i)^{1+\gamma\omega}} \frac{e^{-i\omega r}}{r}, \text{ as } \omega r \rightarrow \infty \\ e^{i\omega r} (\omega r)^\gamma U(1 + \gamma, 2(1 + \gamma), 2i\omega r) & \sim \frac{1}{(2i)^{1+\gamma\omega}} \frac{e^{i\omega r}}{r}, \text{ as } \omega r \rightarrow \infty \end{cases}. \quad (4.44)$$

We note that the above solutions have the correct asymptotic behaviour expected if we fix $\omega > 0$ and take the limit of large $r/2M$. In fact, this can be seen at Fig. 4.5, which also can be seen as a cross check against the expressions above and our asymptotic expression for $R_{\ell\omega}^{up}(r)$ at large r . The solutions maintain good agreement for small ℓ -values, while relatively good pattern agreement is kept throughout ω -values.



(a) $M\omega = 0.01$ & $\ell = 0$.

Figure 4.5: Comparison between $R_{\ell\omega}^{up}(r)$ and $r\omega R(r)$, where $R(r)$ is given by Eq. 4.44, where we took the expression corresponding to the large ωr -limit $e^{i\omega r}/(2i)^{1+\alpha}\omega r$. Continuous curves represent the functions absolute value of the real part, while dashed lines correspond to absolute imaginary. On the other hand, the green color curves show the large ωr asymptote, while blue ones show upgoing modes – calculated with large r -asymptote. We notice the good agreement between them.

4.5.2 Exact solution, $\omega = 0$

We also compare the numerical results to analytical expressions for $\omega = 0$. We follow the work of [82], recognizing, however, that their Eq. 58 is not applicable to our scalar field (spin=0) case. In particular, the aforementioned solutions do not reproduce the necessary radial decay for large r -values.

In fact, we recall that in section 4.2, we obtained that infinity is a regular singular point (only) when $\omega = 0$ in Eq. 4.8. Due to this fact and considering the necessary radial decay, we arrive at the following pair of solutions:

$$\bar{R}_{\ell 0}^{in}(r) = P_{\ell}(r/M - 1) \quad (4.45)$$

$$\bar{R}_{\ell 0}^{up}(r) = \frac{i\pi}{2} P_{\ell}(r/M - 1) + Q_{\ell}(r/M - 1) \quad (4.46)$$

where $P_{\ell}(x)$ and $Q_{\ell}(x)$ are the Legendre Polynomials of order ℓ of first and second kind, respectively.

In Figs. 4.6 and 4.7, we represented Eqs. 4.45 and 4.46 multiplied by a factor $r/2M$ and their comparisons against our solutions $R_{\ell\omega}^{in}(r)$ and $R_{\ell\omega}^{up}(r)$ for a set of small frequencies. In order to perform the graphical comparisons, we choose an ad hoc normalization of the upgoing exact solution, requiring it to have the same norm as the numerical solution for $\omega = 0.01/M$ for one fixed radius.

4.5.3 Small $M\omega$

We have also explored small-frequency expansions for ingoing and upgoing modes that are present on [21]. We find that small $M\omega$ expansions for ingoing modes are in great agreement with our solutions and asymptote for $\omega = 0$. Nevertheless, this was not the case for the series expression for upgoing modes, which – even when extended for a second order contribution – was not able to reproduce the behaviour of either our upgoing modes solutions or asymptote. We understand that this discrepancy is due to our tests being made on an immediate neighborhood of the event horizon, which is a region of slower convergence rate for this specific representation.

4.5.4 Candelas' asymptotics for ℓ -sum

We now explore a result obtained by Candelas [16] as another useful check for our upgoing mode solutions – obtained through numerical integration – and MST coefficients. In this paper, he finds that:

$$\sum_{\ell=0}^{\infty} (2\ell + 1) \left| \overleftarrow{R}_{\ell\omega}(r) \right|^2 \underset{r \rightarrow 2M^+}{\sim} \frac{4\omega^2}{1 - r/2M}, \quad (4.47)$$

where $\overleftarrow{R}_{\ell\omega}(r) \propto R_{\ell\omega}^{in}(r)$ – proportionality factor is given by Eqs. 5.1-5.5.

We would like to emphasize that the left hand side (LHS) of Eq. 4.47 will set out up-

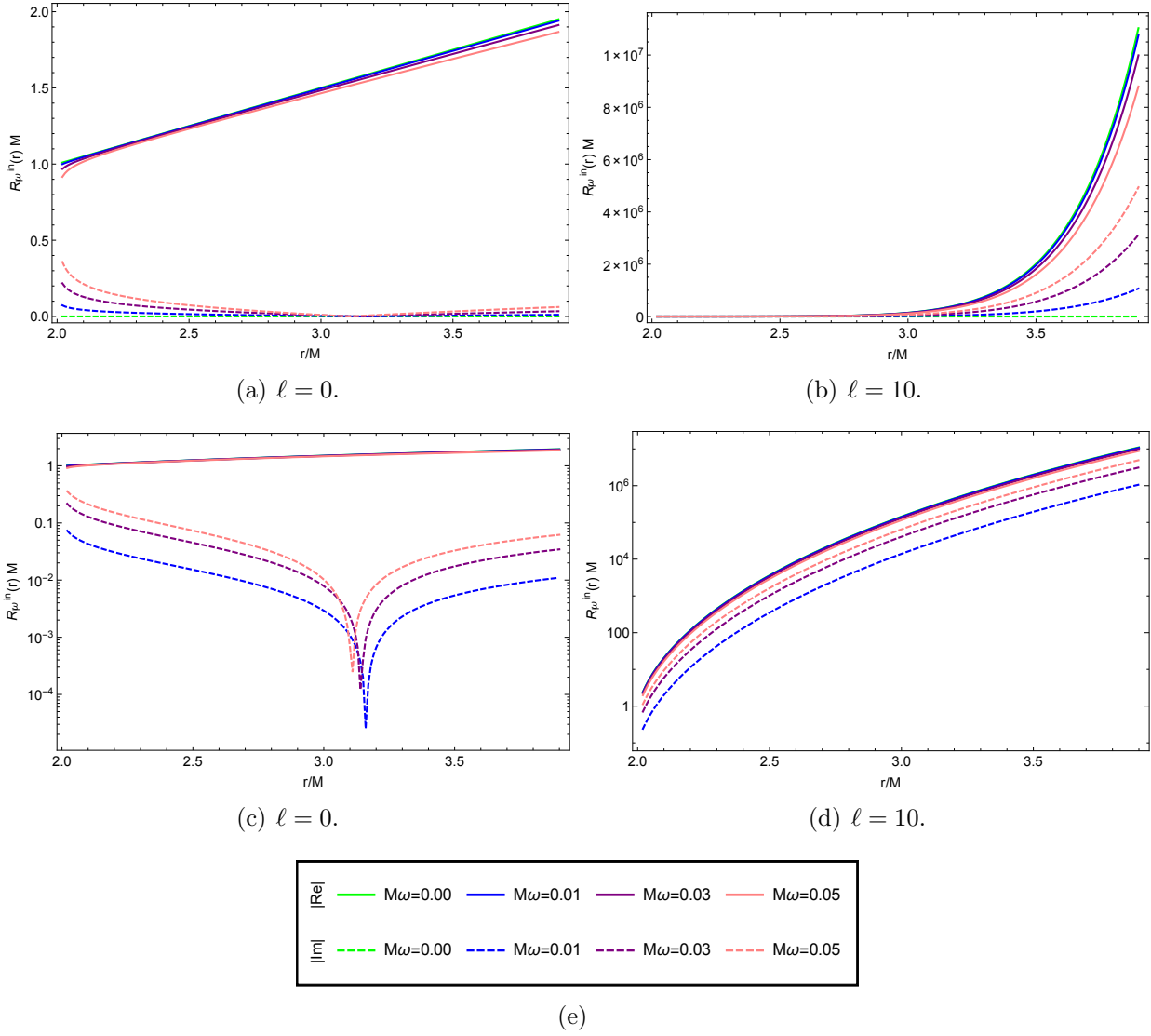


Figure 4.6: Comparison between $R_{\ell\omega}^{in}(r)$ and $R_{\ell 0}^{in}(r)$. Continuous curves represent the functions' absolute value of the real part, while dashed curves correspond to the absolute imaginary part. The green color curves show the exact solution $R_{\ell 0}^{in}(r)$, which in many cases are not visible for being plotted under the solution for $M\omega = 0.01$. We notice the converging behaviour of the small- ω solutions towards the exact solution for $M\omega = 0$.

per bounds in the graphs that follow, since we only considered a limited amount of mode contributions to the (positive definite) sum.

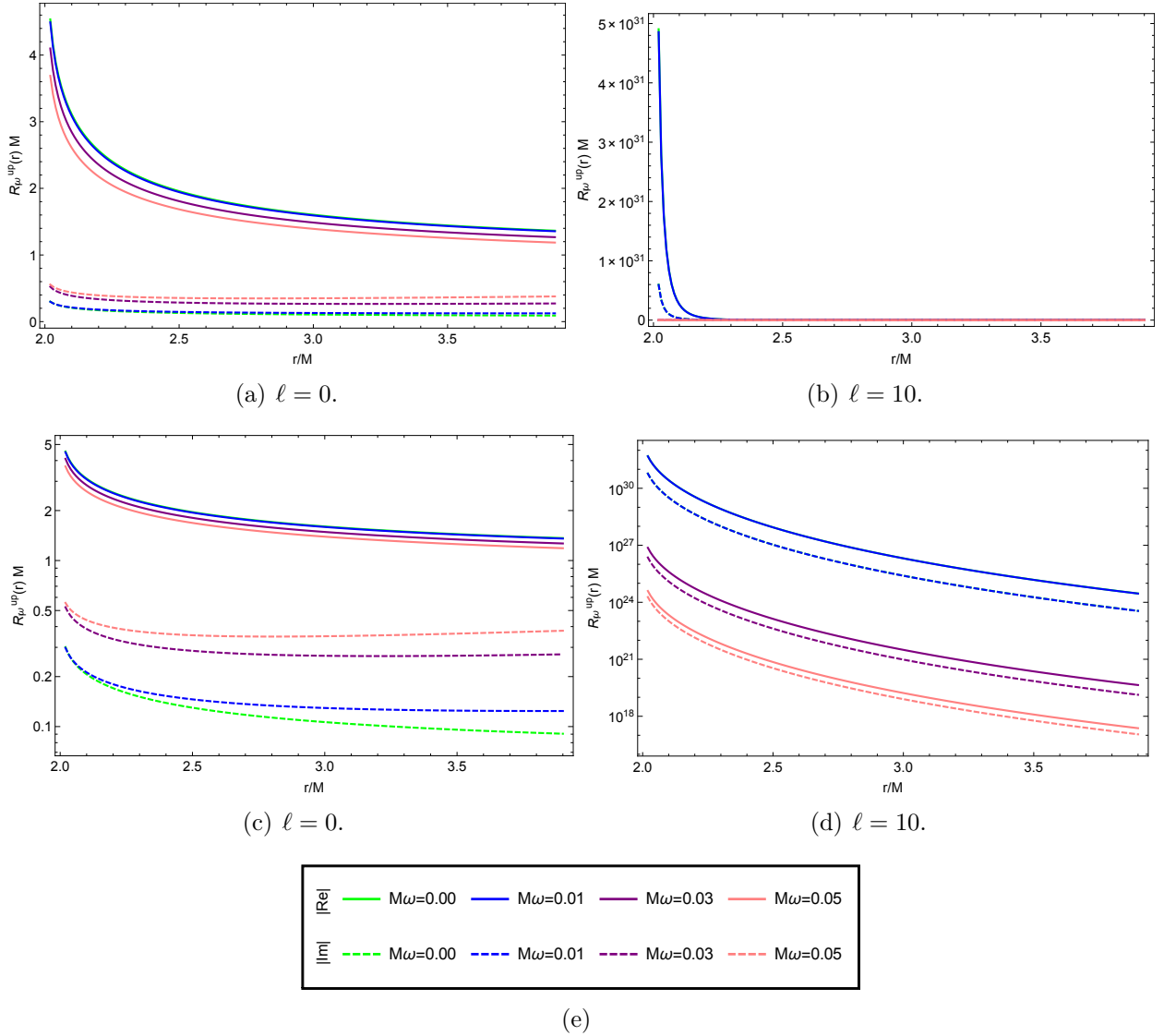


Figure 4.7: Comparison between $R_{l\omega}^{up}(r)$ and $R_{l0}^{up}(r)$. Continuous curves represent the functions' absolute value of the real part, while dashed curves correspond to the absolute imaginary part. The green color curves show the exact solution $R_{l0}^{up}(r)$, which in many cases are not visible for being plotted under the solution for $M\omega = 0.01$. We notice the converging behaviour of the small- ω solutions towards the exact solution for $M\omega = 0$.

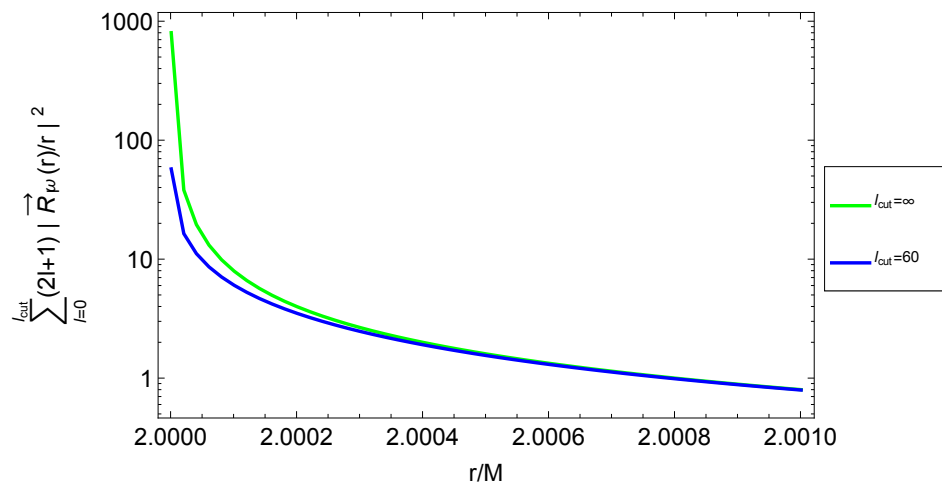
(a) $M\omega = 0.01$.

Figure 4.8: Check using Eq. 4.47 obtained by Candelas. Green curves correspond to the exact asymptotic expression in the RHS of Eq. 4.47, while blue curves correspond to the LHS of this same equation summed up to $\ell = 60$.

Chapter 5

Two-point Correlation Functions

This chapter refers to the numerical calculation of the two-point correlation functions presented in Eqs. 3.9 - 3.11 and a relevant case-study.

This chapter is composed of two sections. The first concerns a general property related to the equality among the integrands in the aforementioned equations and their decay. The second section presents a case-study evincing divergence patterns of these two-point correlation functions and the recovery of a well-established classical result.

We now specify the normalization used in Eqs. 3.9 - 3.11:

$$\vec{R}_{l\omega m} = \begin{cases} e^{i\omega r} + \vec{A}e^{-i\omega r_*}, & r_* \rightarrow -\infty \\ Be^{i\omega r}, & r_* \rightarrow \infty \end{cases} \quad (5.1)$$

and

$$\overleftarrow{R}_{l\omega m} = \begin{cases} Be^{-i\omega r}, & r_* \rightarrow -\infty \\ e^{-i\omega r} + \overleftarrow{A}e^{i\omega r_*}, & r_* \rightarrow \infty \end{cases} \quad (5.2)$$

The B , \vec{A} and \overleftarrow{A} coefficients are expressed as:

$$B = \frac{1}{A_{in}} = \frac{1}{B_{out}} \quad (5.3)$$

$$\vec{A} = \frac{B_{in}}{A_{in}} \quad (5.4)$$

$$\overleftarrow{A} = \frac{A_{out}}{A_{in}}. \quad (5.5)$$

The numerical method implemented in our case-study follows the script:

- we consider $|M\omega|$ within the range $[1/100, 10]$, varying with increments of $\delta\omega = 1/100M$ and $\ell = 0, 1, 2, \dots, 60$;
- calculation of the coefficients in Eqs. 5.3-5.5 is made with the MST method, as in [21];
- calculation of ingoing modes with Jaffé series [19];
- numerical integration (with Mathematica's NDSolve and precision options therein);
- improper integrals are only integrated over the interval $|M\omega| \in [0, 10]$, with the use of interpolation function¹ and Mathematica's Integrate command, along with proper precision requirements.

In order to validate the numerical steps described above, we employ different numerical tests – to do so, we also included extensive use of the property obtained in Section 5.1 and its implications. The different methods described in Chapter 4 are also explored. Finally, our results are consistent with general Physics arguments and this helps to build up on the confidence of the method applied.

5.1 Equality Between the Real Parts

In this section, we study the equality among real parts of the Feynman Green Functions presented in Eq. 3.9 - 3.11. This equality is guaranteed in theory by the expression

$$\text{Re}(G_F(x, x')) = -\frac{1}{2}(G_R(x, x') + G_A(x, x')) = -\frac{1}{2} \begin{cases} G_R(x, x'), & t - t' > 0 \\ G_A(x, x'), & t - t' < 0 \end{cases}, \quad (5.6)$$

which is obtained from Eq. 2.70 - 2.72 of reference [10]. Here t and t' are the Schwarzschild times associated to the spacetime positions x and x' , respectively, and G_R and G_A are the retarded and advanced classical two-point functions – which are defined by the Green function equation² and the requirement of being null when x is outside the causal future

¹It also requires the use of extrapolation function at $M\omega = 0$ when considering the Boulware case or folded integrals. We also point out that this regime is more relevant for late times behaviour.

²The Green function equation is given by $\nabla^\mu \nabla_\mu G_{A/R}(x, x') = \delta^4(x, x')$, where $G_{A/R}(x, x')$ is the Retarded/Advanced Green function at points x and x' , while $\delta^4(x, x')$ is an invariant four-dimensional Dirac delta function.

and past of x' , respectively. From this expression, we can also interpret that the real part of the Feynman functions only carries classical information contained in these two-point correlation functions, while the imaginary contains all the information about the quantum state.

As a first step, we verify analytically that, in fact, this equality throughout states is held already at the integrand level, up to remaining terms, \mathcal{O}_{up} and \mathcal{O}_{in} . We arrive at

$$\begin{aligned} Re(G_B) &= - \sum_{\ell, m} \int_0^\infty \frac{d\omega}{4\pi\omega} Im \left(\vec{u}_{\ell\omega m}(x) \vec{u}_{\ell\omega m}^*(x') + \overleftarrow{u}_{\ell\omega m}(x) \overleftarrow{u}_{\ell\omega m}^*(x') \right) \\ &= \frac{-1}{2i} \sum_{\ell, m} \int_0^\infty \frac{d\omega}{4\pi\omega} \left[\vec{u}_{\ell\omega m}(x) \vec{u}_{\ell\omega m}^*(x') - \vec{u}_{\ell\omega m}^*(x) \vec{u}_{\ell\omega m}(x') \right. \\ &\quad \left. + \overleftarrow{u}_{\ell\omega m}(x) \overleftarrow{u}_{\ell\omega m}^*(x') - \overleftarrow{u}_{\ell\omega m}^*(x) \overleftarrow{u}_{\ell\omega m}(x') \right], \end{aligned}$$

$$\begin{aligned} Re(G_U) &= - \lim_{b, c \rightarrow \infty} \sum_{\ell=0}^c \sum_m \int_0^b \frac{d\omega}{4\pi\omega} Im \left(\frac{\vec{u}_{\ell\omega m}(x) \vec{u}_{\ell\omega m}^*(x')}{1 - e^{-2\pi\omega/\kappa}} + \frac{e^{-2\pi\omega/\kappa}}{1 - e^{-2\pi\omega/\kappa}} \vec{u}_{\ell-\omega m}(x) \vec{u}_{\ell-\omega m}^*(x') \right. \\ &\quad \left. + \overleftarrow{u}_{\ell\omega m}(x) \overleftarrow{u}_{\ell\omega m}^*(x') \right) + \mathcal{O}_{up} \\ &= - \lim_{b, c \rightarrow \infty} \sum_{\ell=0}^c \sum_m \int_0^b \frac{d\omega}{4\pi\omega} Im \left(\frac{\vec{u}_{\ell\omega m}(x) \vec{u}_{\ell\omega m}^*(x')}{1 - e^{-2\pi\omega/\kappa}} + \frac{e^{-2\pi\omega/\kappa}}{1 - e^{-2\pi\omega/\kappa}} \vec{u}_{\ell\omega m}^*(x) \vec{u}_{\ell\omega m}(x') \right. \\ &\quad \left. + \overleftarrow{u}_{\ell\omega m}^*(x) \overleftarrow{u}_{\ell\omega m}(x') \right) + \mathcal{O}_{up} \\ &= Re(G_B) + \mathcal{O}_{up} \end{aligned}$$

and

$$\begin{aligned} Re(G_H) &= - \lim_{b, c \rightarrow \infty} \sum_{\ell=0}^c \sum_m \int_0^b \frac{d\omega}{4\pi\omega} Im \left(\frac{\vec{u}_{\ell\omega m}(x) \vec{u}_{\ell\omega m}^*(x')}{1 - e^{-2\pi\omega/\kappa}} + \frac{e^{-2\pi\omega/\kappa}}{1 - e^{-2\pi\omega/\kappa}} \vec{u}_{\ell-\omega m}(x) \vec{u}_{\ell-\omega m}^*(x') \right. \\ &\quad \left. + \frac{\overleftarrow{u}_{\ell\omega m}^*(x) \overleftarrow{u}_{\ell\omega m}(x')}{e^{2\pi\omega/\kappa} - 1} + \frac{e^{2\pi\omega/\kappa}}{e^{2\pi\omega/\kappa} - 1} \overleftarrow{u}_{\ell-\omega m}^*(x) \overleftarrow{u}_{\ell-\omega m}(x') \right) + \mathcal{O}_{up} + \mathcal{O}_{in} \\ &= - \lim_{b, c \rightarrow \infty} \sum_{\ell=0}^c \sum_m \int_0^b \frac{d\omega}{4\pi\omega} Im \left(\frac{\vec{u}_{\ell\omega m}(x) \vec{u}_{\ell\omega m}^*(x')}{1 - e^{-2\pi\omega/\kappa}} + \frac{e^{-2\pi\omega/\kappa}}{1 - e^{-2\pi\omega/\kappa}} \vec{u}_{\ell\omega m}^*(x) \vec{u}_{\ell\omega m}(x') \right. \\ &\quad \left. + \frac{\overleftarrow{u}_{\ell\omega m}^*(x) \overleftarrow{u}_{\ell\omega m}(x')}{e^{2\pi\omega/\kappa} - 1} + \frac{e^{2\pi\omega/\kappa}}{e^{2\pi\omega/\kappa} - 1} \overleftarrow{u}_{\ell\omega m}(x) \overleftarrow{u}_{\ell\omega m}^*(x') \right) + \mathcal{O}_{up} + \mathcal{O}_{in} \\ &= Re(G_B) + \mathcal{O}_{up} + \mathcal{O}_{in}, \end{aligned}$$

where

$$\mathcal{O}_{up} = - \lim_{a,b,c \rightarrow \infty} \sum_{\ell=0}^c \sum_m \int_{-a}^{-b} \frac{d\omega}{4\pi\omega} \text{Im} \left(\frac{\vec{u}_{\ell\omega m}(x) \vec{u}_{\ell\omega m}^*(x')}{1 - e^{-2\pi\omega/\kappa}} \right)$$

and

$$\mathcal{O}_{in} = - \lim_{a,b,c \rightarrow \infty} \sum_{\ell=0}^c \sum_m \int_{-a}^{-b} \frac{d\omega}{4\pi\omega} \text{Im} \left(\frac{\overleftarrow{u}_{\ell\omega m}^*(x) \overleftarrow{u}_{\ell\omega m}(x')}{e^{2\pi\omega/\kappa} - 1} \right).$$

From now on, we call ‘‘folded integrands’’ the integrands obtained from Eqs. 3.9 - 3.11 after a change of the integration range ($\int_{-\infty}^{\infty} \mapsto \int_0^{\infty}$) through the same methods as applied in the above equations. We denote these folded integrands as g_{\bullet} , where \bullet labels the quantum state (Boulware, Unruh, Hartle-Hawking). On the other hand, we denote f_{\bullet} the integrands of Eqs. 3.9 - 3.11 in their original form.

We now extend this analysis by taking a closer look at the remaining terms, \mathcal{O}_{up} and \mathcal{O}_{in} . In order to do that, we use Eq. 4.38, along with the relevant normalization and the relation $|\vec{A}|^2 - 1 = -|B|^2$, thus, obtaining:

$$\begin{aligned} \vec{u}_{\ell\omega m}(x) \vec{u}_{\ell\omega m}^*(x') &= \left[\frac{\vec{A}}{B} \overleftarrow{u}_{\ell\omega m}(x) + \frac{1}{B^*} \overleftarrow{u}_{\ell\omega m}^*(x) \right] \left[\frac{\vec{A}}{B} \overleftarrow{u}_{\ell\omega m}(x') + \frac{1}{B^*} \overleftarrow{u}_{\ell\omega m}^*(x') \right]^* \\ &= \left| \frac{\vec{A}}{B} \right|^2 \overleftarrow{u}_{\ell\omega m}(x) \overleftarrow{u}_{\ell\omega m}^*(x') + \frac{1}{|B|^2} \overleftarrow{u}_{\ell\omega m}^*(x) \overleftarrow{u}_{\ell\omega m}(x') \\ &\quad + \frac{\vec{A}}{B^2} \overleftarrow{u}_{\ell\omega m}(x) \overleftarrow{u}_{\ell\omega m}(x') + \left[\frac{\vec{A}}{B^2} \overleftarrow{u}_{\ell\omega m}(x) \overleftarrow{u}_{\ell\omega m}(x') \right]^* \end{aligned} \quad (5.7)$$

and

$$\text{Im} (\vec{u}_{\ell\omega m}(x) \vec{u}_{\ell\omega m}^*(x')) = \frac{|\vec{A}|^2 - 1}{|B|^2} \text{Im} (\overleftarrow{u}_{\ell\omega m}(x) \overleftarrow{u}_{\ell\omega m}^*(x')) = -\text{Im} (\overleftarrow{u}_{\ell\omega m}(x) \overleftarrow{u}_{\ell\omega m}^*(x')), \quad (5.8)$$

which applied to the expressions for \mathcal{O}_{up} and \mathcal{O}_{in} – after performing a change of variables

($\omega \mapsto -\omega$) and using the property $\vec{u}_{\ell, -\omega, -m}(x) = \vec{u}_{\ell\omega m}^*(x)$ – results on the upper bounds:

$$\begin{aligned} |\mathcal{O}_{up}| &= \left| \lim_{a,b,c \rightarrow \infty} \sum_{l=0}^c \sum_m \int_a^b \frac{d\omega}{4\pi\omega} \text{Im} \left(\frac{\vec{u}_{\ell\omega m}^*(x) \vec{u}_{\ell\omega m}(x')}{e^{2\pi\omega/\kappa} - 1} \right) \right| \\ &\leq \left| \lim_{a,b,c \rightarrow \infty} \frac{1}{4\pi a} \frac{1}{e^{2\pi a/\kappa} - 1} \sum_{l=0}^c \sum_m \int_a^b d\omega \text{Im} (\vec{u}_{\ell\omega m}^*(x) \vec{u}_{\ell\omega m}(x')) \right| \end{aligned} \quad (5.9)$$

and

$$\begin{aligned} |\mathcal{O}_{in}| &= \left| \lim_{a,b,c \rightarrow \infty} \sum_{l=0}^c \sum_m \int_a^b \frac{d\omega}{4\pi\omega} \text{Im} \left(\frac{\vec{u}_{\ell\omega m}(x) \vec{u}_{\ell\omega m}^*(x')}{1 - e^{-2\pi\omega/\kappa}} \right) \right| \\ &\leq \left| \lim_{a,b,c \rightarrow \infty} \frac{1}{4\pi a} \frac{1}{1 - e^{-2\pi a/\kappa}} \sum_{l=0}^c \sum_m \int_a^b d\omega \text{Im} (\vec{u}_{\ell\omega m}(x) \vec{u}_{\ell\omega m}^*(x')) \right|. \end{aligned} \quad (5.10)$$

From the above expressions, we can also conclude that $\mathcal{O}_{up} < \mathcal{O}_{in}$, therefore, it is suffice to show that \mathcal{O}_{in} equals to zero, as expected. In fact, this is the case as can be proved when we consider Eq. 5.8 and the large ωr asymptotic obtained in the previous chapter, Eq. 4.44.

Notice that the inequalities in expressions 5.10 and 5.9 are obtained assuming $0 \leq a \leq b$. Nevertheless, the results do not change if $b \leq a$, one only needs to replace a by b , due to the fact that we are considering absolute values.

We add that, in the case-study that follows, we have numerically tested the integrand-level equality of the real part of the Feynman Green Functions. These tests resulted in relative errors of the order similar to the initial minimum precision requested in the calculation of the mode solutions.

5.2 Case-study: Singularity Structure and Caustics

In this section, we once more make use of the identity given by Eq. 5.6, exploring a well-studied result in the literature. We first present and discuss the intermediary graphical results related to numerical calculations and, then, do the same for the physical outcomes of this case-study.

Here, the two-point correlation functions (Eqs. 3.9 - 3.11) are calculated with one fixed spacetime point, x (with $r = 6M$ and, without loss of generality, arbitrary values of time

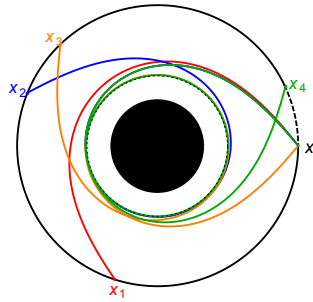


Figure 5.1: We display, in black, a circular geodesic orbit of radius $r = 6M$ and frequency $\Omega = \sqrt{M/r^3}$. The first four null geodesics that start at point x and re-intersect the orbit to the past of x are displayed in colourful lines. Finally, the dashed black curve represents the photon sphere ($r = 3M$). Image credit: [20].

and angular coordinates), and the other point, x' , at different times along a timelike circular geodesic of the same radius. In other words, we compute the two-point functions for $r = r' = 6M$, $\Delta\theta = 0$ and $\Delta\phi(\Delta t) = \sqrt{M/r^3}\Delta t$, while considering a time span of $\Delta t = t - t' \in (15M, 85M)$. This scenario is shown in Fig. 5.1, along with the first four null geodesics (colourful curves) that depart from the spacetime point x and re-intersect the circular geodesic of radius $r = 6M$.

In Fig. 5.2, we show the behaviour of the logarithm of the absolute value of real and imaginary parts of the integrands of Eq. 3.9 - 3.11 (g_B , f_U and f_H , respectively) as a function of both ω and ℓ , with Δt fixed at $\Delta t = 40M$). Although these graphs do not support absolute convergence of the integrals – which was not expected –, they do favour the application of smoothing functions. This is so because applying a smoothing in ω automatically causes a smoothing-cut in ℓ , due to the decay of the integrands' absolute value in an increasing area around the ℓ -axis – see, in particular, Fig. 5.2 (a). This property takes great importance due to the relevance of smoothing techniques on Quantum Field Theory.

In this same scenario, Fig. 5.3 show the integrands of Eq. 3.9 - 3.11 as functions of ω . Here, curves of different colors represent different values of ℓ . In these graphs, we already can see the influence of the thermal factor, $1/(1 - e^{-8\pi M\omega})$, in the two-point functions' expressions.

Similarly to the previous case, in Fig. 5.4 we split the contributions of ingoing and upgoing modes to the absolute value of these integrands. We can draw a few conclusions from these graphs, which are:

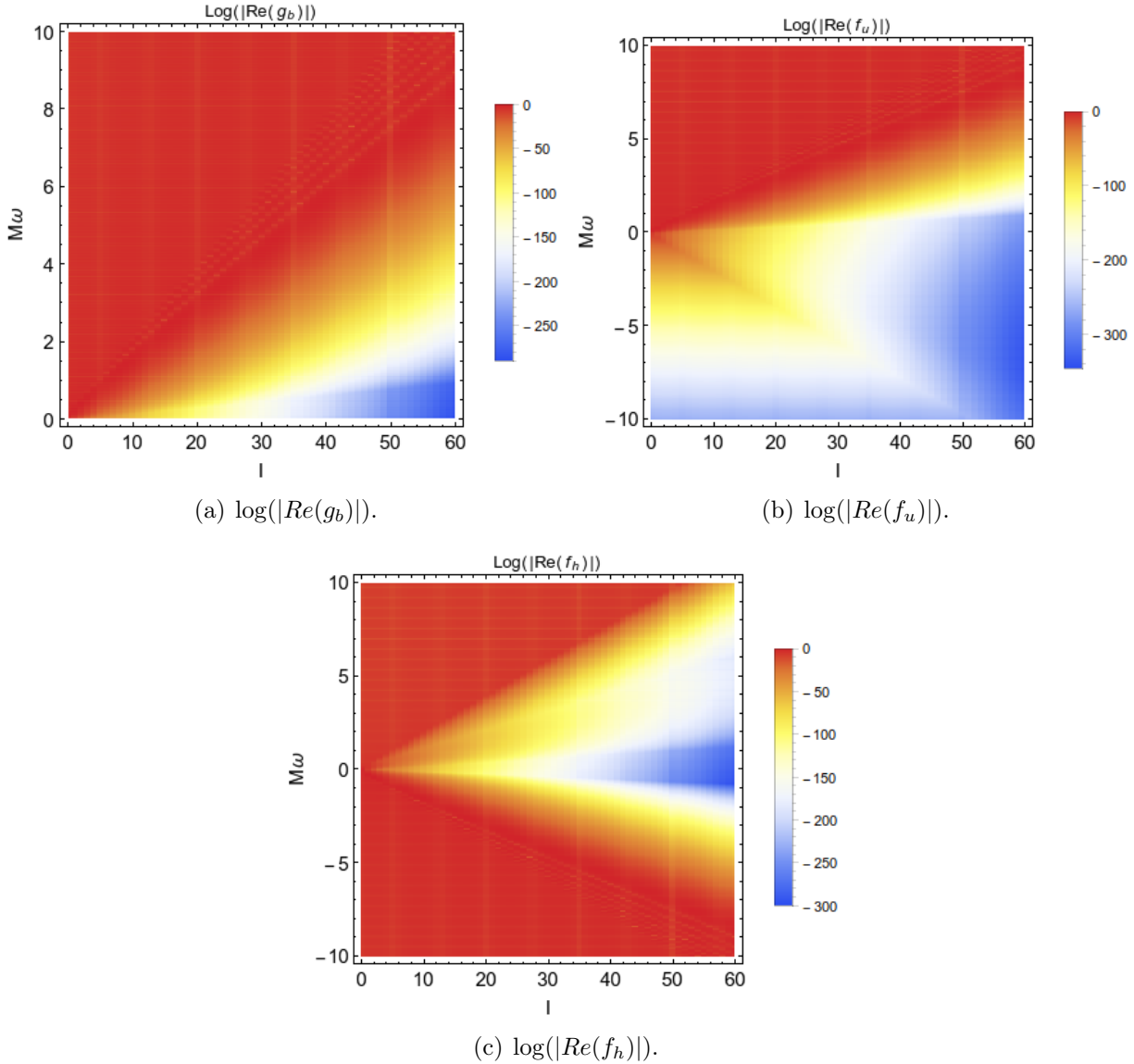
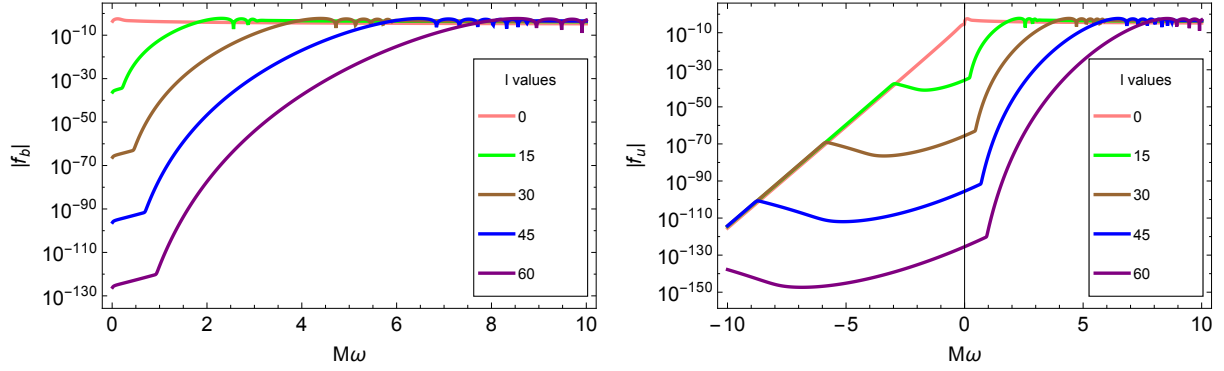


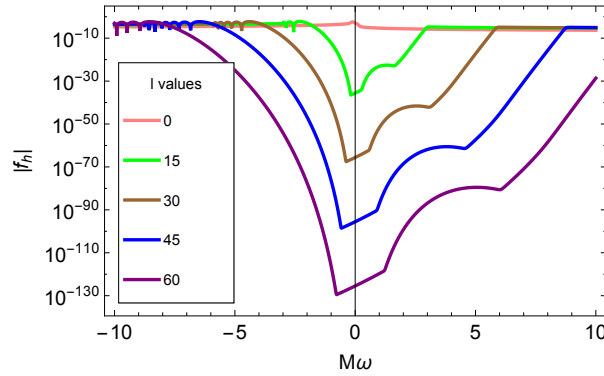
Figure 5.2: Density graphs presenting the logarithm behaviour of real parts for the integrands of Eqs. 3.9 - 3.11 as a function of the frequency, ω , and angular momentum, ℓ . The corresponding graphs for the imaginary parts do not show significant differences, therefore, we omit them from this presentation. Finally, we note that when we consider the folded integrands, g_\bullet , all of them produce a similar behaviour to that seen in (a). Therefore, they favour the use of ω -smoothing functions, due to the decay behaviour concentrated around ℓ -axis. Snapshot at $\Delta t = 40M$.

- We can see that in- and upgoing contributions to the integrands peak at a certain value of $M\omega$ and that this effect is even more pronounced in the case of the upgoing contribution. We have numerically found that, for a given value of ℓ , this maximum occurs at $\omega = V_{max}^{1/2}$, where V_{max} is the maximum value of the effective-potential given by Eq. 4.5. These extremum-dependences on $M\omega$ and ℓ – and their stronger behaviour for upgoing contributions – are expected from the interpretation of the Regge-Wheeler potential working as a barrier for the penetration and reflection of in- and outgoing



(a) Absolute value of the integrand for the Boulware two-point function.

(b) Absolute value of the integrand for the Unruh two-point function.



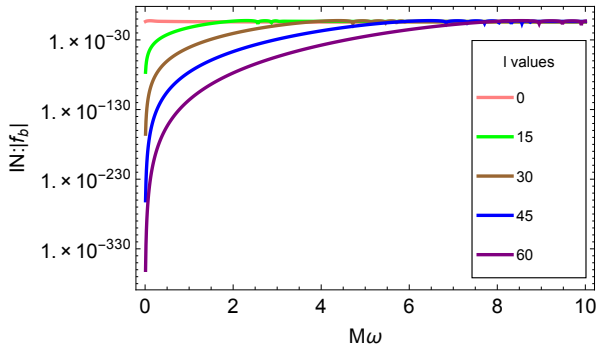
(c) Absolute value of the integrand for the Hartle-Hawking two-point function.

Figure 5.3: Log-plots showing the behaviour of the absolute value of the integrands (f_b , f_u and f_h) of Eqs. 3.9 - 3.11 as a function of ω . Curves in different colors correspond to different values of ℓ . We note that the folded integrands (g_u and g_h) will behave similarly to what is shown in (a).

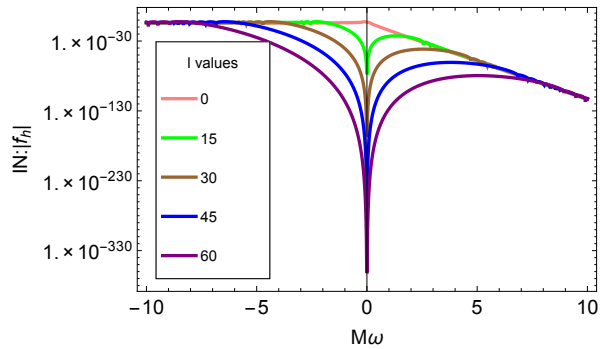
modes;

- Upgoing modes have a more intense contribution to the integrands than the ingoing modes, in this regime – at the Inner most Stable Circular Orbit (ISCO), $r = 6M$ – for positive frequencies, see the difference in the orders of magnitude;
- Figs. 5.4 (d) explicitly shows the effect of the thermal factor, $1/(1 - e^{-8\pi M\omega})$, on the upgoing contribution to the integrands, in special in the negative $M\omega$ -regime;
- Similarly, Fig. 5.4 (b) shows the influence of the factor $1/(e^{8\pi M\omega} - 1)$ multiplying the ingoing contribution, specially in the positive $M\omega$ regime;
- We conclude the analysis of Fig. 5.4 noticing that the graphical behaviour in (a) is shared by the Boulware and Unruh states and (d) is shared by Unruh and Hartle-

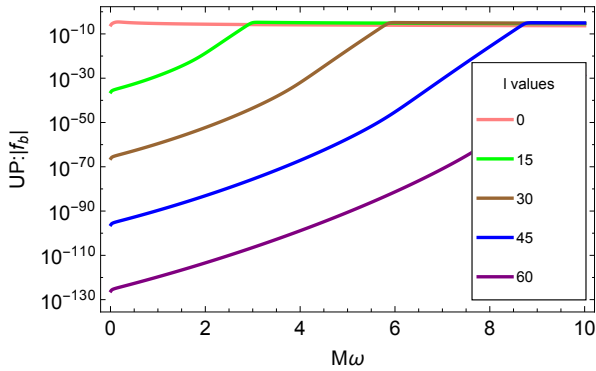
Hawking states, since the corresponding expressions are exactly the same.



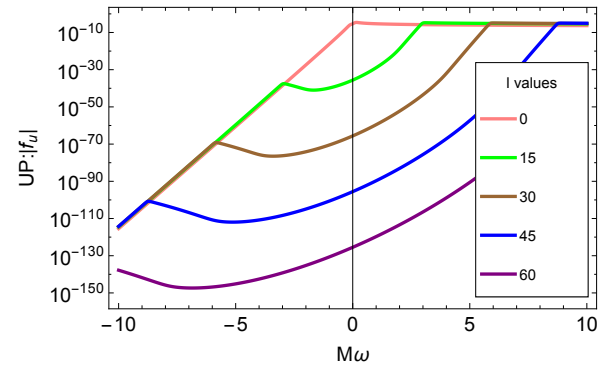
(a) Graph showing the ingoing contribution to the integrands for the Boulware or Unruh states (since they have the same formal dependence). Notice the considerably smaller order of magnitude compared to that in (c).



(b) Graph showing the ingoing contribution to the Hartle-Hawking state integrands. Notice the influence of the factor multiplying the ingoing contribution, specially on the positive ω -regime.



(c) Graph showing the upgoing contribution to the integrands for the Boulware state.



(d) Graph showing the upgoing contribution to the integrands for the Unruh or Hartle-Hawking states (since they have the same formal dependence). Notice the influence of the thermal factor, specially on the negative ω regime.

Figure 5.4: *Graphs showing the contributions of ingoing and upgoing modes, separately, for the integrands for each state as functions of ω with different curve colors representing different choices of ℓ .*

We now focus on the resulting computation of Eqs. 3.9 - 3.11. Fig. 5.5 illustrates different features of wave propagation on a Schwarzschild background, such as the fact that the Green functions diverge whenever x' and x are connected via a null geodesic [41; 50]. In fact, this was observed before in [20] using the Retarded Green Function and, here, we illustrate it using the Feynman Green Function for the Unruh quantum state – we omit the results for Boulware and Hartle-Hawking due to their similarity to the Unruh case (this similarity is better understood after our analysis of the divergence patterns shown in Fig. 5.5).

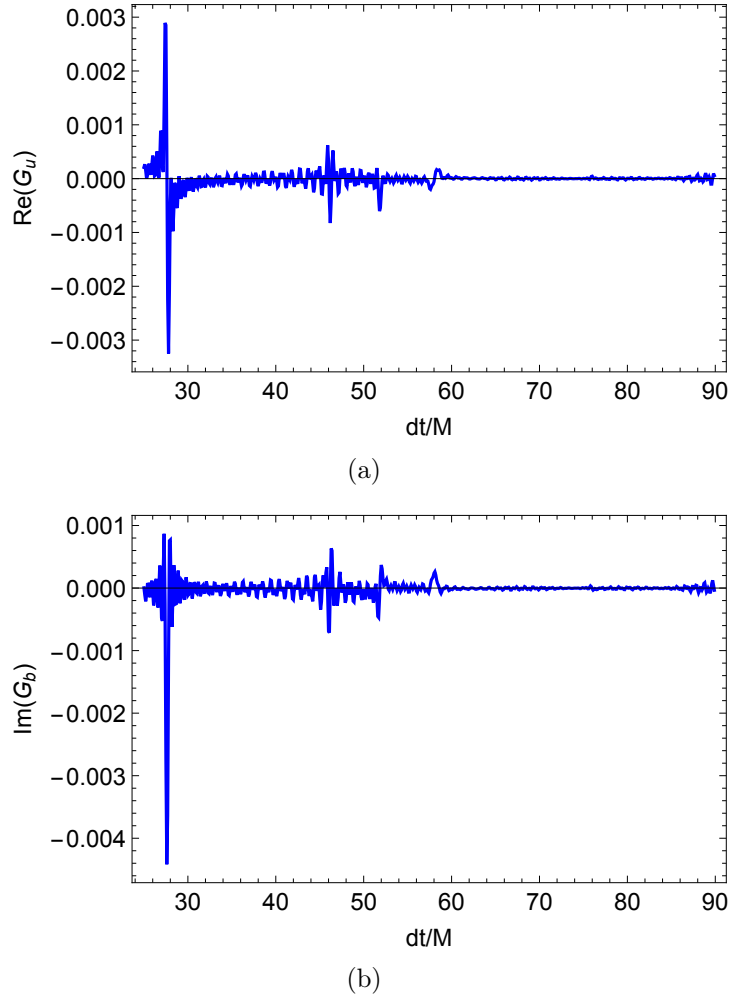


Figure 5.5: Real and imaginary part of Unruh two-point correlation function along a circular geodesic orbit. The peaks occur on the exact spacetime point where null geodesics crossings occur (see Fig 5.1) – this time regime shows the first four of these intersections. The ℓ -sum is performed up to $\ell_{cut} = 60$, patterns shown here do not change significantly with larger ℓ_{cut} .

Moreover, it is of fundamental importance to the establishment of the numerical implementation of Eqs. 3.9 - 3.11 that the divergences shown in Fig. 5.5 have, indeed, the same qualitative behaviour as those obtained by means of the calculation of the Retarded Green function, such as the divergences’ four-fold pattern, as demonstrated in [20].

In fact, the Hadamard form explicitly presents the divergence of a Green function when the two space-time points are connected by a null geodesic. It is, however, valid only when the points are connected by a unique geodesic³. For the Feynman Green function, the Hadamard

³A “direct” null geodesic occurs when the unique geodesic is lightlike. In the example given in Fig. 5.1, the only “direct” null geodesic is the red curve that joins x and x_1 .

form is (e.g., [72]⁴)

$$G_F(x, x') = \lim_{\epsilon \rightarrow 0^+} \frac{-i}{2\pi} \left[\frac{U(x, x')}{\sigma + i\epsilon} - V(x, x') \ln(\sigma + i\epsilon) + W(x, x') \right], \quad (5.11)$$

where $U(x, x')$, $V(x, x')$ and $W(x, x')$ are regular and real-valued biscalars. The σ function is Synge's world function and is equal to⁵ one-half of the square of the geodesic distance along a geodesic joining x and x' . We note that while $U(x, x')$ and $V(x, x')$ are determined *uniquely* by the geometry of the space-time, $W(x, x')$ is not.

The following distributional properties are useful:

$$\lim_{\epsilon \rightarrow 0^+} \frac{1}{\sigma + i\epsilon} = \text{P.V.} \left(\frac{1}{\sigma} \right) - i\pi\delta(\sigma), \quad (5.12)$$

where P.V. denotes the Cauchy principal value distribution, and

$$\lim_{\epsilon \rightarrow 0^+} \ln(\sigma + i\epsilon) = \ln|\sigma| + i\pi\theta(-\sigma). \quad (5.13)$$

When using Eqs.5.12, 5.13 and 5.6, Eq.5.11 implies that the Hadamard form for the retarded Green function is given by

$$G_R(x, x') = [U(x, x')\delta(\sigma) + V(x, x')\theta(-\sigma)]\theta_+(x, x'), \quad (5.14)$$

where $\theta_+(x, x')$ equals 1 if x' belongs to the causal future of x and is equal to 0 otherwise.

As already mentioned, the Hadamard form is not valid when more than one geodesic joins the points x and x' , which is generally the case when the points are “far enough” in a curved spacetime – as in the Schwarzschild case. Nevertheless, the divergence of the retarded Green function for *arbitrary* null-separated points in Schwarzschild space-time has been obtained recently (see [22] and references therein). It has been found that the divergence of G_R follows

⁴We note that we use a convention where the source in the wave equation satisfied by the Feynman Green function is ‘ $-\delta^{(4)}(x - x')/\sqrt{|g|}$ ’. This source differs by a sign from the convention of [72] and from the source of the retarded and advanced Green functions in this thesis.

⁵We note that the world function σ is strictly well-defined only in the region of validity of the Hadamard form, since it is no longer uniquely defined when there is more than one geodesic joining two points. However, by indicating along which geodesic σ is measured, this object can effectively be extended to any pairs of points in Schwarzschild space-time – see [22] for details. It is in this extended sense that we are using σ .

a 4-fold pattern (except at caustic points, which are points where neighbouring null geodesics focus). In particular, the pattern for the leading divergence in G_R is given by

$$\delta(\sigma) \rightarrow \text{PV}(1/\sigma) \rightarrow -\delta(\sigma) \rightarrow -\text{PV}(1/\sigma) \rightarrow \delta(\sigma) \rightarrow \dots \quad (5.15)$$

while for the sub-leading divergence it is

$$\theta(-\sigma) \rightarrow -\ln|\sigma| \rightarrow -\theta(-\sigma) \rightarrow \ln|\sigma| \rightarrow \theta(-\sigma) \rightarrow \dots \quad (5.16)$$

The singularity type changes as the null wavefront passes through caustic points. Referring again to Fig. 5.1, this means that the leading singularity of G_R at x_1 will be $\delta(\sigma)$, at x_2 it will be $\text{PV}(1/\sigma)$, at x_3 it will be $-\delta(\sigma)$ and at x_4 it will be $-\text{PV}(1/\sigma)$; the subleading singularity will respectively be $\theta(-\sigma)$, $-\ln|\sigma|$, $-\theta(-\sigma)$ and $\ln|\sigma|$.

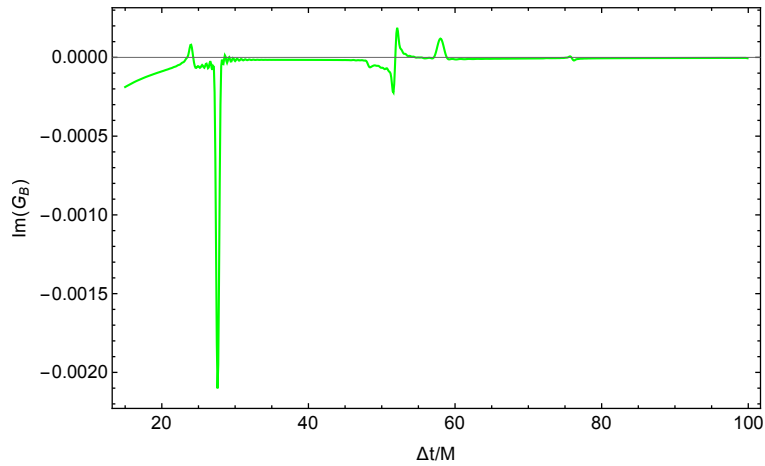
As opposed to the Retarded Green function case (which can be obtained from the real part of the Feynman Green function), to the best of our knowledge, the *global* singularity structure of the imaginary part of the Feynman Green function in Schwarzschild space-time has not yet been obtained.

We now refer to Fig. 5.6 (a) and (b), where we show what the divergence structure for the imaginary part of the Feynman Green function is. We note that it displays the same pattern as the four-fold singularity structure in Eq.5.15, but shifted by one period:

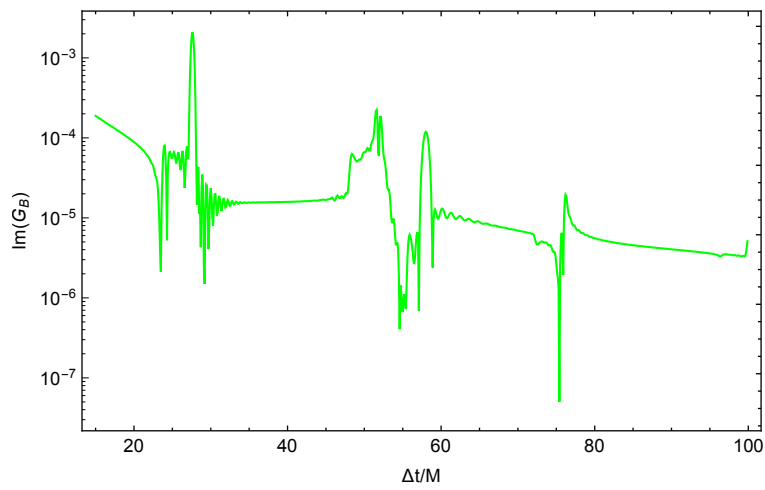
$$\text{PV}(1/\sigma) \rightarrow -\delta(\sigma) \rightarrow -\text{PV}(1/\sigma) \rightarrow \delta(\sigma) \rightarrow \text{PV}(1/\sigma) \rightarrow \dots \quad (5.17)$$

The Hadamard form Eq.5.11, with Eq. 5.12, only provides the first term in Eq.5.17. On the other hand, it was conjectured in [17; 18; 22] that the global structure for the imaginary part of the Feynman Green function would be as in Eq.5.17. This conjecture was based on the fact that $U(x, x')$ obeys a transport equation along a geodesic and that it picks up a phase of $-\pi/2$ as the geodesic crosses a caustic point [17]. We argue that Fig. 5.6 provides a numerical corroboration of this conjecture.

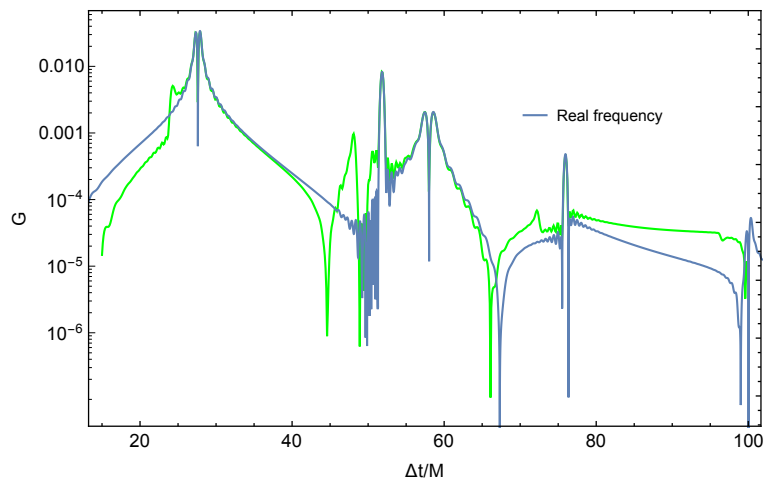
In Fig. 5.6 (c), we show a log-plot of the retarded Green function from [20] together with our calculation of the real part of the Feynman Green function, where smoothing functions



(a) Imaginary part of the smoothed Boulware Green function. Notice the four-fold patterns.



(b) Log-plot for the absolute value of the imaginary part of the smoothed Boulware Green function.



(c) Log-plot showing the Retarded Green Function (blue) as obtained in [20] and the real part of the two-point correlation function (green).

Figure 5.6: Graphs showing the results for the Boulware Green function. Notice that in (c) the divergences' regions show excellent agreement when comparing both methods.

were applied (as in the case for Fig. 5.6 (a) e (b)). We point out that, although the behaviour in the in-between-peaks regions is not well predicted by our method, the agreement regarding the divergences' location is excellent. We argue, therefore, that our method traces well the occurrence of the divergences, while still in need of work (probably on fine-tuning the choice of smoothing function and cutoffs and improving the numerical accuracy of our calculations) in the intermediary regions.

Chapter 6

Conclusions

In this dissertation we have presented a brief review on classical and quantum black holes, which included an overview of General Relativity and Quantum Field Theory on Curved Spacetimes. We have also presented two chapters containing relevant results to this dissertation, Chapters 4 and 5. The first included results related to mode decomposition of a free scalar field equation on Schwarzschild spacetime. The second one, in its turn, contains results focused on general properties and the calculation of Feynmann Green Functions for the Boulware, Unruh and Hartle-Hawking quantum states.

In Chapter 4 we have revisited known results in the literature [25; 68], such as the separability of the massless scalar wave equation with mode-like Ansatzes, the study of the singular points of the radial differential equation in the Ingoing/Outgoing Eddington-Finkelstein coordinate systems and series representations for its solutions. We have also discussed the different methods used to calculate these modes in the exterior region of the event horizon for the in-, out- and upgoing boundary conditions presented. In Appendix A, we present numerical tests for our mode solutions.

We implemented a prescription by Damour and Ruffini [31] in order to continue to $r \in (0, 2M)$ our calculation of the modes outside the horizon. In fact, to the best of our knowledge, this has been the first time that upgoing modes have been implemented in the interior of the Schwarzschild black hole. We have also analysed the divergent behaviour of the in- and outgoing modes as they approach the curvature divergence of the Schwarzschild spacetime, $r = 0$. The final section of that chapter presents a variety of asymptotic and

exact solutions which we obtained *inspired* by works present in the literature [28; 82] and graphical comparisons.

The relevance of Chapter 4 is three-fold: (i) the methods described in Sec. 4.4 are used later in Chapter 5 for the calculation of the Feynman two-point functions; (ii) the establishment of independent methods for the calculation of the radial function and the obtention of asymptotic and exact solutions built up on our confidence that the methods applied in the literature and here are both correct – in special for the upgoing modes; and (iii) with the extension of radial functions to the interior of the black hole, we start to pave the way for studying correlations across the event horizon in a Schwarzschild spacetime.

In Chapter 5 we discuss the calculation of the Feynman Green functions, properties and one case-study. Among other properties, we show that the real part of the two-point function is indeed the same for the three states, as expected from the general theory of QFT CS, and we check that this is indeed the case for the specific numerical calculation that we carried out.

In our case-study in Chapter 5, we resort to the equality of real parts of Feynman Green functions and of the Retarded Green function. Here, we were able to numerically verify this relation and a conjuncture [18; 22] regarding a four-fold pattern in the global divergence structure of the Feynman Green function. In this same section, we also present graphical results that illustrate properties related to smoothing techniques and to the isolated contributions by in- and upgoing modes to the correlation functions' integrands.

We believe that conclusions drawn in this case-study and the extension of modes across the event horizon are essential to the establishment of our calculation of the correlation functions, representing another building block to the study of correlations across the event horizon.

Appendix A

Numerical Tests

We have thoroughly numerically tested the mode solutions in order to guarantee numerical accuracy. We summarize some of these tests in Table A.1. Comparisons are made between numerically integrated mode solutions (and derived quantities) and method pointed out in the ‘‘Comparison Against’’ column.

Table A.1: *Numerical Tests*

Object	Region	Comparison Against	Worst Discrepancy
$\Psi_{\omega l}^{in}$	Exterior	Series, Eq. 4.35 with $\alpha = 0$	$\mathcal{O}[10^{-19}]$
$\Psi_{\omega l}^{in}$	Exterior	Numerical Integration as in [88]	$\mathcal{O}[10^{-29}]$
$\Psi_{\omega l}^{in}$	Exterior	Jaffé Series [19]	$\mathcal{O}[10^{-25}]$
$\Psi_{\omega l}^{in}$	Exterior	LHS of Eq. 4.8 = 0	$\mathcal{O}[10^{-37}]$
$\Psi_{\omega l}^{in'}$	Exterior	Derivative Eq.4.35 with $\alpha = 0$	$\mathcal{O}[10^{-17}]$
$\Psi_{\omega l}^{up}$	Exterior	Numerical Integration as in [88]	$\mathcal{O}[10^{-29}]$
$\Psi_{\omega l}^{up}$	Exterior	Jaffé Series [19]	$\mathcal{O}[10^{-17}]$
$\Psi_{\omega l}^{up}$	Exterior	LHS of Eq. 4.8 = 0	$\mathcal{O}[10^{-37}]$
$W(\Psi_{\omega l}^{in}, \Psi_{\omega l}^{up})$	Exterior	$W'(R_{\omega l}^{in}, R_{\omega l}^{up}) = 0$	$\mathcal{O}[10^{-29}]$
$W(\Psi_{\omega l}^{out}, \Psi_{\omega l}^{up})$	Exterior	$W'(R_{\omega l}^{in}, R_{\omega l}^{up}) = 0$	$\mathcal{O}[10^{-30}]$
$\Psi_{\omega l}^{in}$	Interior	Series, Eq. 4.35 with $\alpha = 0$	$\mathcal{O}[10^{-21}]$
$\Psi_{\omega l}^{in}$	Interior	LHS of Equation 4.8 = 0	$\mathcal{O}[10^{-34}]$
$\Psi_{\omega l}^{in'}$	Interior	Derivative of Eq.4.35 with $\alpha = 0$	$\mathcal{O}[10^{-22}]$
$\Psi_{\omega l}^{out}$	Interior	Numerical Integration as in [88]	$\mathcal{O}[10^{-19}]$
$\Psi_{\omega l}^{out}$	Interior	LHS of Eq. 4.8 = 0	$\mathcal{O}[10^{-34}]$
$\Psi_{\omega l}^{out'}$	Interior	Derivative of Eq. 4.37	$\mathcal{O}[10^{-21}]$
$W(R_{\omega l}^{in}, R_{\omega l}^{up})$	Interior	$W'(R_{\omega l}^{in}, R_{\omega l}^{up}) = 0$	$\mathcal{O}[10^{-29}]$
$W(R_{\omega l}^{out}, R_{\omega l}^{up})$	Interior	$W'(R_{\omega l}^{out}, R_{\omega l}^{up}) = 0$	$\mathcal{O}[10^{-30}]$

The comparison against ‘‘LHS of Eq. 4.8 = 0’’ takes the numerically obtained solutions and their derivatives and reintroduce them into the left hand side of Eq. 4.8 in order to see if

the equality in this equation still holds. Similarly, we check if the derivative of the Wronskian in respect to the tortoise coordinate is null in the test with the objects $W(R_{\omega l}^{\bullet}, R_{\omega l}^{up})$, where \bullet stands for *in* or *out*.

Notice that for these particular tests we have chosen precision setting to be of order 20.

Bibliography

- [1] B. P. Abbott and et al. Observation of Gravitational Waves from a Binary Black Hole Merger. *Phys. Rev. Lett.*, 116(6):061102, 2016. 7
- [2] T.L. Ainsworth and et al. *Recent Progress in Many-Body Theories*. Number v. 3. Springer US, 2012. 18
- [3] A. Almheiri and et al. An apologia for firewalls. *Journal of High Energy Physics*, 9:18, September 2013. 1, 21
- [4] Ahmed Almheiri and et al. Black Holes: Complementarity or Firewalls? *JHEP*, 02:062, 2013. 1, 21
- [5] AQFT in nLab. <https://ncatlab.org/nlab/show/AQFT>, Release 1.0.11 of 2016-06-08, 2015. (Accessed on 2015-07-01). 23
- [6] G. B. Arfken and et al. *Mathematical Methods for Physicists: A Comprehensive Guide*. Elsevier, 2013. 29, 30, 31
- [7] A. K. Baczkó and et al. A Highly Magnetized Twin-Jet Base Pinpoints a Supermassive Black Hole. *ArXiv e-prints*, May 2016, 1605.07100. 11
- [8] F. Belgiorno and et al. Hawking Radiation from Ultrashort Laser Pulse Filaments. *Physical Review Letters*, 105(20):203901, November 2010. 2, 22
- [9] H. R. Beyer. On the stability of the massive scalar field in Kerr space-time. *Journal of Mathematical Physics*, 52(10):102502–102502, October 2011. 19
- [10] N. D. Birrell and et al. *Quantum Fields in Curved Space*. Cambridge Monographs on Mathematical Physics. Cambridge University Press, 1984. 13, 15, 50
- [11] D. G. Boulware. Spin- $\frac{1}{2}$ quantum field theory in schwarzschild space. *Phys. Rev. D*, 12:350–367, Jul 1975. 19
- [12] R. H. Brandenberger. Introduction to Early Universe Cosmology. *PoS*, ICFI2010:001, 2010, 1103.2271. 2
- [13] A. E. Broderick and et al. On the Nature of the Compact Dark Mass at the Galactic Center. *ApJ*, 638:L21–L24, February 2006, astro-ph/0512211. 11
- [14] A. E. Broderick and et al. The Event Horizon of M87. *Astrophys. J.*, 805(2):179, 2015. 11
- [15] C. Buss and et al. Study of a scalar field on the maximally extended schwarzschild spacetime. *Journal of Physics: Conference Series*, 689(1):012002, 2016. 17, 39, 40

- [16] P. Candelas. Vacuum polarization in schwarzschild spacetime. *Phys. Rev. D*, 21:2185–2202, Apr 1980. 19, 20, 44
- [17] M. Casals and et al. Self-force calculations with matched expansions and quasinormal mode sums. *Phys. Rev. D*, 79:124043, Jun 2009. 60
- [18] M. Casals and et al. Branch cut and quasinormal modes at large imaginary frequency in schwarzschild space-time. *Phys. Rev. D*, 86:024021, Jul 2012. 4, 60, 64
- [19] M. Casals and et al. Analytic Investigation of the Branch Cut of the Green Function in Schwarzschild Space-time. *Phys. Rev.*, D87(6):064010, 2013. 35, 39, 50, 65
- [20] M. Casals and et al. Self-force and Green function in Schwarzschild spacetime via quasinormal modes and branch cut. *Phys. Rev. D*, 88(4):044022, August 2013. xiv, 3, 54, 57, 58, 60, 61
- [21] M. Casals and et al. High-order tail in Schwarzschild spacetime. *Phys. Rev. D*, 92(12):124055, December 2015. 39, 44, 50
- [22] M. Casals and et al. Global Hadamard form for the Green Function in Schwarzschild space-time. *ArXiv e-prints*, June 2016, 1606.03075. 4, 59, 60, 64
- [23] J. Casares and et al. A Be-type star with a black-hole companion. *Nature*, 505:378–381, January 2014, 1401.3711. 10
- [24] S. Chakraborty and et al. Quantum leaps of black holes: Magnifying glasses of quantum gravity. *ArXiv e-prints*, June 2016, 1606.04348. 1, 21
- [25] S. Chandrasekhar. *The mathematical theory of black holes*. Oxford classic texts in the physical sciences. Oxford Univ. Press, Oxford, 2002. 14, 26, 63
- [26] S. Chatrchyan and et al. Observation of a new boson at a mass of 125 GeV with the CMS experiment at the LHC. *Physics Letters B*, 716:30–61, September 2012. 18
- [27] Y. Choquet-Bruhat. *General Relativity and the Einstein Equations*. Oxford Mathematical Monographs. OUP Oxford, 2008. 5
- [28] S. Creek and et al. Greybody factors for brane scalar fields in a rotating black-hole background. *Phys. Rev.*, D75:084043, 2007. 41, 64
- [29] M. Dafermos and et al. Decay for solutions of the wave equation on Kerr exterior spacetimes III: The full subextremal case $|a| \leq M$. *ArXiv e-prints*, February 2014, 1402.7034. 19
- [30] D. Dalvit and et al. *Casimir Physics*. Lecture Notes in Physics. Springer Berlin Heidelberg, 2011. 18
- [31] T. Damour and et al. Black-hole evaporation in the klein-sauter-heisenberg-euler formalism. *Phys. Rev. D*, 14:332–334, Jul 1976. 3, 17, 37, 63
- [32] H. Dennhardt and et al. Scalar deformations of Schwarzschild holes and their stability. *Int. J. Mod. Phys.*, A13:741–764, 1998, gr-qc/9612062. 19
- [33] NIST Digital Library of Mathematical Functions. <http://dlmf.nist.gov/>, Release 1.0.11 of 2016-06-08, 2015. Online companion to [64]. 41, 42, 70

- [34] J. F. Dolan. Dying pulse trains in cygnus xr-1: Evidence for an event horizon? *Publications of the Astronomical Society of the Pacific*, 113(786):974, 2001. 10, 11
- [35] C. J. Fewster. Lectures on quantum field theory in curved spacetime. Technical report, Max Planck Institute for Mathematics in the Sciences, 2008. 13
- [36] F. Finster and et al. *Quantum Field Theory and Gravity: Conceptual and Mathematical Advances in the Search for a Unified Framework*. Springer Basel, 2012. 15
- [37] L. H. Ford. Quantum Field Theory in Curved Spacetime. *ArXiv General Relativity and Quantum Cosmology e-prints*, July 1997, gr-qc/9707062. 13, 19
- [38] V. Frolov and et al. *Black Hole Physics: Basic Concepts and New Developments*. Fundamental Theories of Physics. Springer Netherlands, 2012. 13
- [39] V. P. Frolov and et al. *Introduction to Black Hole Physics*. OUP Oxford, 2011. xiii, 9, 13, 17
- [40] S. A. Fulling. *Aspects of Quantum Field Theory in Curved Spacetime*. London Mathematical Society Student Texts. Cambridge University Press, 1989. 13
- [41] P. Garabedian. *Partial Differential Equations*. AMS Chelsea Publishing Series. Chelsea Publishing Company, 1986. 57
- [42] J. B. Hartle and et al. Path-integral derivation of black-hole radiance. *Phys. Rev. D*, 13:2188–2203, Apr 1976. 20
- [43] S. W. Hawking. Black hole explosions? *Nature*, 248:30–31, March 1974. 1
- [44] S. W. Hawking. Particle creation by black holes. *Communications in Mathematical Physics*, 43:199–220, August 1975. 1, 21
- [45] S. W. Hawking. Breakdown of predictability in gravitational collapse. *Phys. Rev. D*, 14:2460–2473, Nov 1976. 1, 21
- [46] S. W. Hawking and et al. *The Large Scale Structure of Space-Time*. Cambridge Monographs on Mathematical Physics. Cambridge University Press, 1973. 5
- [47] S. W. Hawking and et al. Soft hair on black holes. *Phys. Rev. Lett.*, 116:231301, Jun 2016. 1, 21
- [48] S. Hossenfelder and et al. Conservative solutions to the black hole information problem. *Phys. Rev. D*, 81:064009, Mar 2010. 1, 21
- [49] R. A. Hulse. The discovery of the binary pulsar. *Rev. Mod. Phys.*, 66:699–710, Jul 1994. 7
- [50] M. Ikawa. *Hyperbolic Partial Differential Equations and Wave Phenomena*. Number v. 2 in Iwanami series in modern mathematics. American Mathematical Society, 2000. 57
- [51] T. Jacobson. Introduction to Quantum Fields in Curved Spacetime and the Hawking Effect. *ArXiv General Relativity and Quantum Cosmology e-prints*, August 2003, gr-qc/0308048. 2

- [52] R. Johnston. List of black hole candidates. <http://www.johnstonsarchive.net/relativity/bhtable.html>, Jan 2004. (Accessed on 10/05/2016). 11
- [53] B. S. Kay and et al. Linear stability of schwarzschild under perturbations which are non-vanishing on the bifurcation 2-sphere. *Classical and Quantum Gravity*, 4(4):893, 1987. 19
- [54] M. D. Kruskal. Maximal extension of schwarzschild metric. *Phys. Rev.*, 119:1743–1745, Sep 1960. 9
- [55] E. Kuulkers and et al. MAXI J1659-152: the shortest orbital period black-hole transient in outburst. *A & A*, 552:A32, April 2013, 1204.5840. 10
- [56] O. Lahav and et al. Realization of a Sonic Black Hole Analog in a Bose-Einstein Condensate. *Physical Review Letters*, 105(24):240401, December 2010. 2, 22
- [57] E. W. Leaver. Solutions to a generalized spheroidal wave equation: Teukolsky’s equations in general relativity, and the two-center problem in molecular quantum mechanics. *Journal of Mathematical Physics*, 27:1238–1265, May 1986. 35
- [58] Z. Li and et al. Evidence for A Parsec-scale Jet from The Galactic Center Black Hole: Interaction with Local Gas. *Astrophys. J.*, 779:154, 2013. 11
- [59] M. Martellini and et al. Comment on the damour-ruffini treatment of black-hole evaporation. *Phys. Rev. D*, 15:2415–2416, Apr 1977. 17, 37
- [60] J. M. Martín-García. xAct: Efficient tensor computer algebra for the Wolfram Language. <http://www.xact.es/>, 2002-2016. 26
- [61] G. Menezes. Radiative processes of two entangled atoms outside a Schwarzschild black hole. *ArXiv e-prints*, December 2015. 19
- [62] C. W. Misner and et al. *Gravitation*. Number pt. 3 in Gravitation. W. H. Freeman, 1973. 5
- [63] W. Naylor and et al. Dynamical Casimir effect for TE and TM modes in a resonant cavity bisected by a plasma sheet. *Phys. Rev. A*, 80(4):043835, October 2009. 18
- [64] F. W. J. Olver and et al, editors. *NIST Handbook of Mathematical Functions*. Cambridge University Press, New York, NY, 2010. Print companion to [33]. 68
- [65] A. Ori. Structure of the singularity inside a realistic rotating black hole. *Phys. Rev. Lett.*, 68:2117–2120, Apr 1992. 2
- [66] R. Parentani. From vacuum fluctuations across an event horizon to long distance correlations. *Phys. Rev. D*, 82:025008, Jul 2010. 2
- [67] R. Parentani and et al. Hawking radiation. http://www.scholarpedia.org/article/Hawking_radiation, 2011. (Accessed on 10/01/2016). 19
- [68] D. Philipp and et al. On analytic solutions of wave equations in regular coordinate systems on Schwarzschild background. March 2015. 26, 28, 63
- [69] E. Poisson and et al. Internal structure of black holes. *Phys. Rev. D*, 41:1796–1809, Mar 1990. 2

- [70] J. Rammer. *Quantum Field Theory of Non-equilibrium States*. Cambridge University Press, 2007. 18
- [71] M. P. Ryan. Teukolsky equation and penrose wave equation. *Phys. Rev. D*, 10:1736–1740, Sep 1974. 26
- [72] DeWitt B. S. and et al. Radiation damping in a gravitational field. *Ann. Phys*, 0:220, Feb 1960. 59
- [73] J. B. Hartle S. Chandrasekhar. On crossing the cauchy horizon of a reissner-nordstrom black-hole. *Proceedings of the Royal Society of London. Series A, Mathematical and Physical Sciences*, 384(1787):301–315, 1982. 2
- [74] M. Sasaki and et al. Analytic Black Hole Perturbation Approach to Gravitational Radiation. *Living Reviews in Relativity*, 6, November 2003. 2, 3, 17, 39
- [75] R. Schützhold and et al. Quantum correlations across the black hole horizon. *Phys. Rev. D*, 81:124033, Jun 2010. 2
- [76] J. Steinhauer. Observation of self-amplifying Hawking radiation in an analog black hole laser. *Nature Phys.*, 10:864, 2014. 2, 22
- [77] J. H. Taylor. Binary pulsars and relativistic gravity. *Rev. Mod. Phys.*, 66:711–719, Jul 1994. 7
- [78] T. N. Ukwatta and et al. Sensitivity of the FERMI Detectors to Gamma-Ray Bursts from Evaporating Primordial Black Holes (PBHs). *ArXiv e-prints*, March 2010, 1003.4515. 1
- [79] W. G. Unruh. Notes on black-hole evaporation. *Phys. Rev. D*, 14:870–892, Aug 1976. 20
- [80] W. G. Unruh. Experimental black-hole evaporation? *Phys. Rev. Lett.*, 46:1351–1353, May 1981. 1, 22
- [81] W. G. Unruh. Has Hawking radiation been measured? *Found. Phys.*, 44:532–545, 2014. 2, 22
- [82] M. van de Meent and et al. Metric perturbations produced by eccentric equatorial orbits around a Kerr black hole. *Phys. Rev.*, D92(6):064025, 2015. 43, 64
- [83] H. S. Vieira and et al. Acoustic black holes: massless scalar field analytic solutions and analogue Hawking radiation. *Gen. Rel. Grav.*, 48(7):88, 2016. 1, 22
- [84] M. Visser. Acoustic black holes: horizons, ergospheres and Hawking radiation. *Classical and Quantum Gravity*, 15:1767–1791, June 1998, gr-qc/9712010. 1, 22
- [85] R. M. Wald. *General Relativity*. University of Chicago Press, 1984. 5, 6, 16
- [86] R. M. Wald. The Thermodynamics of Black Holes. *Living Rev. Relativity*, 4(6), 2001. (Accessed on 21/05/2016). 1, 22
- [87] R. M. Wald. The Formulation of Quantum Field Theory in Curved Spacetime. *ArXiv e-prints*, July 2009, 0907.0416. 14

- [88] B. Wardell and et al. Self-force via green functions and worldline integration. *Phys. Rev. D*, 89:084021, Apr 2014. [65](#)
- [89] S. Weinfurtner and et al. Measurement of stimulated hawking emission in an analogue system. *Phys. Rev. Lett.*, 106:021302, Jan 2011. [2](#), [22](#)
- [90] B. F. Whiting. Mode Stability of the Kerr Black Hole. *J. Math. Phys.*, 30:1301, 1989. [19](#)
- [91] C. M. Will. The Confrontation between general relativity and experiment. *Living Rev. Rel.*, 9:3, 2006. [7](#)